Chapter 2

Observing the Electromagnetic Spectrum

2.1 Earth's Atmosphere and Extraneous Radiation

Not all photons emitted by astronomical objects are detected by ground-based telescopes. A major barrier to the photons path is the Earth's ionosphere and upper atmosphere that absorbs or scatters most incoming radiation except for the optical (wavelengths of 3300-8000Å where 1 Å = 10^{-10} m), parts of the Near-IR (0.8 - 7 μm) and radio (greater than 1 mm) regions. Absorption greatly affects radiation with the shortest wavelengths. In general, Gamma rays are absorbed by atomic nuclei, X-rays by individual atoms and UV radiation by molecules. Incoming IR and submillimeter radiation are strongly absorbed by molecules in the upper atmosphere (e.g. H_2O and carbon monoxide, CO). Observations in these regions greatly benefit by locating telescopes at high altitude. Mountain top sites like Mauna Kea (altitude 4200 m) in Hawaii, Cerro Pachon (2700 m), Las Campanas (2500 m) and Paranal (2600 m) in Chile, La Palma (2300 m) in the Canary Islands are used to decrease the blocking effect of the atmosphere. The Antarctic, in particular the South Pole, provides an atmosphere with low water vapor content. Most of the continent is at high altitude, with the South Pole 2,835 m above sea level, again helping to reduce the amount of obscuring atmosphere. The Antarctic has therefore also become a very useful IR and submillimeter site.

The transmission properties of the Earth's atmosphere (Figure 2.1) has prompted the exploration of Gamma ray, X-ray, UV, Mid- and Far-IR regions of the electromagnetic spectrum via satellite and high-altitude balloon observations. Satellite observations in the optical (e.g. Hubble Space Telescope) have benefited from being above the majority of the atmosphere allowing near-diffraction limited observations. Radio astronomy satellites have benefited from large distance instrumental baselines. HALCA (Highly Advanced Laboratory for Communications and Astronomy), known as Haruka after launch, operated from 1997 to 2003. It was an 8 m diameter radio telescope used for Very Long Baseline Interferometry. An elliptical orbit (21,400 by
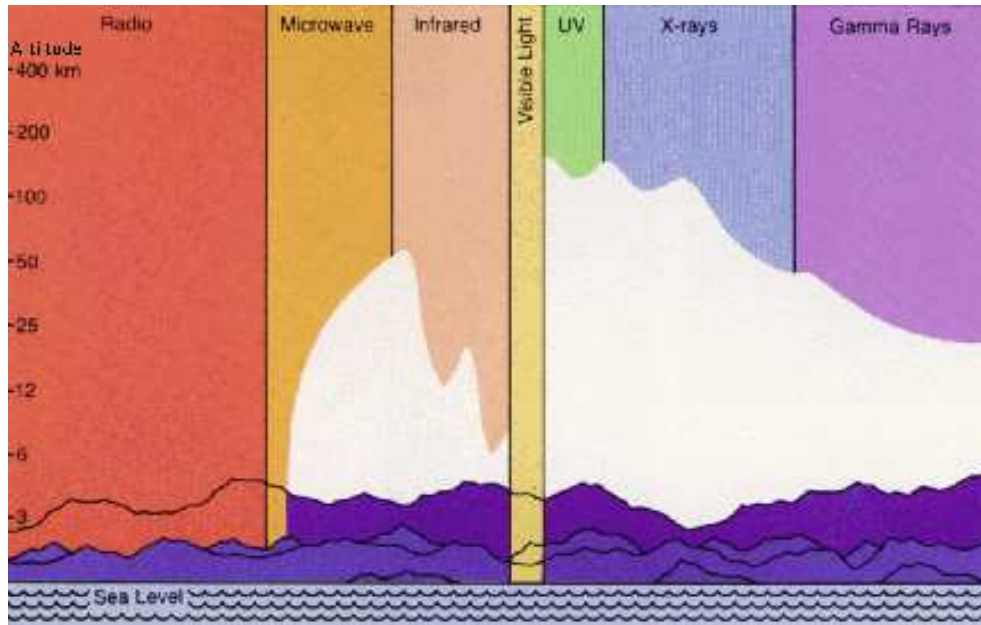
Figure 2.1: Transmission Properties of Earth's Atmosphere. Credit: NASA and "Imagine the Universe!" http://imagine.gsfc.nasa.gov/.

560 km) allowed imaging by the satellite and ground based telescopes, with good (u,v) plane coverage and high resolution. In late 1998 the Balloon Observations of Millimetric Extragalactic Radiation and Geophysics experiment (BOOMERANG), observed the sky at millimeter wavelengths for about ten days. Future space interferometry missions include ESAs Darwin mission and NASAs Terrestrial Planet Finder, both in mission concept stages of planning.

Emission from the night sky plays an important part in observational astronomy and seriously affects our ability to detect faint objects. Reactions in the upper atmosphere that result in radiation are known as *airglow* or *nightglow*. Electrons recombining with ions (e.g. O, Na, O_2, OH) at typical altitudes of 100 km can radiate in the Ultraviolet, optical and Near-IR regions. The emission is usually measured in Rayleighs where

$$1 \text{ Rayleigh} = 10^6 \text{ photons cm}^{-2} \text{ s}^{-1} \text{ sr}^{-1}$$

and sr is steradian[1]. For example, at 762 nm the emission from O_2 is $\sim$6000 Rayleigh.

The interaction of the solar wind with the Earth's magnetic field results in polar *aurorae*, usually close to the geomagnetic poles. Dust grains in the plane of the Solar System scatter sunlight causing *zodiacal light*. The Sun and the Moon are major contributors to night sky brightness. The influence of the Moon is easy to witness if you compare the night sky brightness at both Full and New Moon. Optical observations that aim to detect very faint objects are usually scheduled during dark skies, close to New Moon.

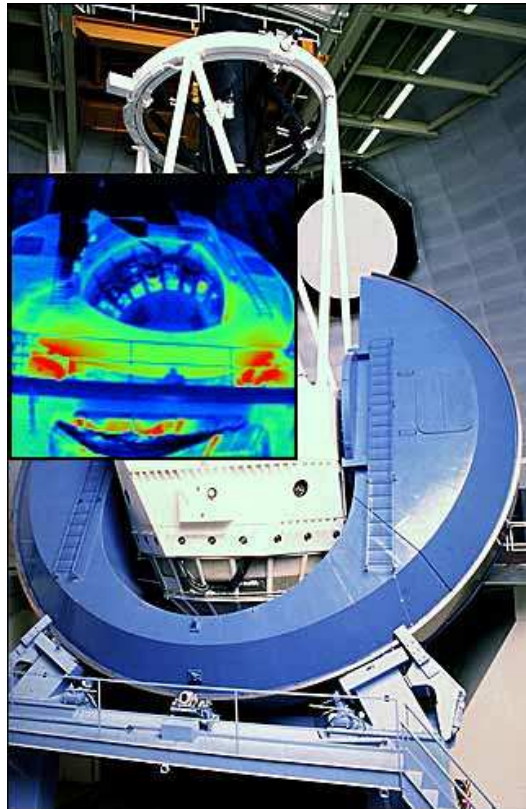[1]Steradian is a unit of solid angle. A sphere measures 4π $\sim$12.56637 steradians

Figure 2.2: The main image shows the Mayall 4 m telescope at Kitt Peak National Observatory in visual light. The insert shows the horseshoe mount at 10 μm taken with a thermal video camera. Hot oil lubricated bearings that support the mount appear as bright red. Credit: National Optical Astronomy Observatory, M. Hanna, G. Jacoby.

Other extraneous radiation sources are also present. Ground-based Near-IR observations are plagued by background heat radiation from the telescope (e.g. mirrors) and structure (e.g. oil lubricated bearing of horseshoe mounts; Figure 2.2). The insert image of Figure 2.2 at a wavelength of 10 μm shows temperature changes represented by color differences. Oil lubricated bearings that support the horseshoe mount appear in the infrared image as bright red, representing a 15° C increase in temperature above surrounding structures.

This nuisance radiation is also minimized by cooling and reducing the surface area along the optical path of instruments. The Near-IR background sky is also very bright and highly variable on short time scales. Observations from the excellent ground-based IR sites of the Antarctic, Chile and Mauna Kea can help minimize such fluctuations, yet satellite observations offer the best IR observing conditions.

Human activity produces spurious radiation sources that can affect astronomical observations. These include microwave and radio emission from industrial and telecommunication sources. In the optical region night-time outdoor lighting and general city and suburban lights have all put additional pressure on the quality of observations. Finally, whilst satellites have allowed us to make observations across
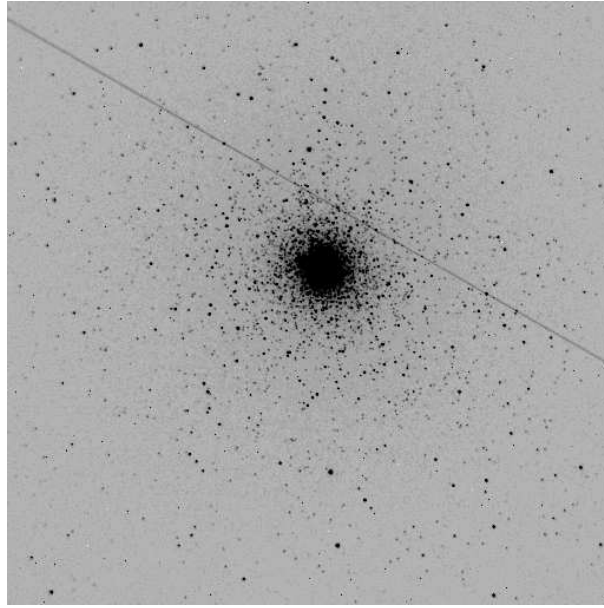
Figure 2.3: Globular cluster NGC 104 (47 Tuc) and satellite trail. A 30 second exposure, 30″ across. Credit: A. Mattingly, Grove Creek Observatory.

the entire electromagnetic region, they too are sources of increasing 'pollution' for ground-based observations, when recorded as streaks of light across long exposure wide-field images near to, or through (Figure 2.3) objects of interest. Of July, 2009 there were ∼900 operational satellites, with ∼1500 objects greater than 100 kg in mass in orbit, and 19,000 objects in orbit with diameters > 10 cm.

2.2　Temperature, Energy, Wavelength and Frequency

In astronomy, temperatures are usually quoted in terms of degrees Kelvin (K). One K is the same interval as 1° Celsius (C), however the Kelvin scale starts at absolute zero, or -273.16° C.

As might be expected temperatures of astronomical radiation sources vary widely. Dusty, dark nebulae (e.g. the Horsehead Nebula in Orion) exist at temperatures between 10-100 K enabling molecular hydrogen (H_2), carbon monoxide (CO), hydrogen cyanide (HCN) and water (H_2O) to exist in molecular clouds.

Dust grains emit at a characteristic temperature between 20-100 K and are found in and near such clouds. The temperature of neutral or atomic hydrogen, H I, is usually between 25-250 K. Emission nebulae or ionized H II regions (near hot, young stars that strongly emit UV radiation) exist at ∼10,000 K. The surface temperatures of stars range from 2,500-40,000 K. Our Sun, a G dwarf, has a surface temperature of 5,800 K. Surface temperatures of neutron stars could be several × 10^5 K. Gas temperatures in accretion disks (e.g. around the black hole candidate Cygnus X-1) are ∼2 × 10^6 K. Galaxy cluster (ICM) gas detected in the X-ray region, typically has

temperatures of 10^7 K. The temperature of gas involved in thermonuclear explosions near the surface of accreting neutron stars is $\sim 10^{7-9}$ K. Hence astronomical object temperatures range over nine orders of magnitude, or a factor of a billion.

Emission, especially in the Gamma ray and X-ray regions, is typically measured in terms of its corresponding energy in units of electron Volts (eV[2]). X-ray energies are usually measured in terms of keV with kT as the symbol for energy, where the k (in kT) is Boltzmann's constant = 1.38 x 10^{-16} erg/K. Gamma ray energies are quoted in MeV, GeV and in extreme cases TeV.

Radiation wavelengths are typically quoted when discussing the EUV region and longer wavelengths. Nanometers (nm) and Angstroms (Å) are used until the Near-IR when microns (μm) are stated. From submillimeter to Radio units progress from mm to cm to m and are interchanged with frequency units such as MHz and GHz.

---

[2]One eV is the energy acquired by an electron when it is accelerated through a potential difference of 1 Volt in a vacuum. 1 eV has an associated energy = 1.60 x 10^{-12} erg.

Table 2 describes the key events in multiwavelength observations of galaxies beginning with Janskys detection of radio emission from the Galaxy in 1931.

Table 2: Key Events in Multiwavelength Observations of Galaxies

Year	Event
1931-1933	Jansky detects radio emission from the Galaxy
1939	Reber detects the radio source Cygnus A
1943	Seyfert identifies six spiral galaxies with broad emission lines
1949	Identification of radio sources Virgo A (with Messier 87) and Centaurus A (NGC 5128) by Bolton, Stanley and Slee
1951	Discovery of 21 cm emission from interstellar hydrogen by Ewen and Purcell
1954	Baade and Minkowski identify the optical counterpart of Cygnus A
1961	Explorer XI satellite detects Gamma rays
1962-1966	Aerobee rockets detect X-ray sources (including Messier 87)
1963	Identification of Quasars
1967	Gamma ray Bursts (GRBs) detected by Vela satellites
late 1960s	First major IR survey by Neugebauer and Leighton detects $\sim$6000 Near-IR sources
1968-1972	OAO series of satellites detect UV sources
1978-1980	HEAO-2 (Einstein) increases number of extragalactic X-ray sources
1983	IRAS performs sky survey at 12, 25, 60 and 100 μm
1985	Antonucci and Miller discover Sy 2 NGC 1068 has broad emission lines (similar to Sy 1s) in polarized light
1987	James Clerk Maxwell Telescope (JCMT) opens
1990	Launch of Hubble Space Telescope, ROSAT
1991	Launch of Compton Gamma ray Observatory (re-entered in 2000)
1992	mm observations by COBE detects 30 μKelvin deviations in the Cosmic Background Radiation
1995	Hubble Deep Field-North observations, ISO launched
1997	Distance scale to GRBs determined via X-ray, Gamma ray and optical observations
1999	Launch of Chandra X-ray Observatory, XMM-Newton
2001	2MASS Near-IR survey ends (began 1997)
2003	Wilkinson Microwave Anisotropy Probe (WMAP) 1st Data Release, Spitzer Space Telescope and GALEX launched
2004	Swift launched
2008	Fermi Gamma ray Space Telescope launched
2009	Herschel Space Observatory launched

2.3 Telescopes and Instruments

The following will briefly describe the main telescopes and instruments used to obtain images presented in the atlas or those used in observations discussed in the text. Detectors are not described. Since there exists significant overlap between telescopes used for submillimeter and radio observations these are considered together.

2.3.1 Gamma ray

kT > 500 keV.

The Compton Gamma Ray Observatory (CGRO; Figure 2.4) was launched into an Earth orbit at 450 km altitude on April 5th, 1991 and re-entered on June 4th, 2000. CGRO contained instruments that could detect radiation with energies from 15 keV to 30 GeV and it was the second of NASA's 'Great Observatories'.
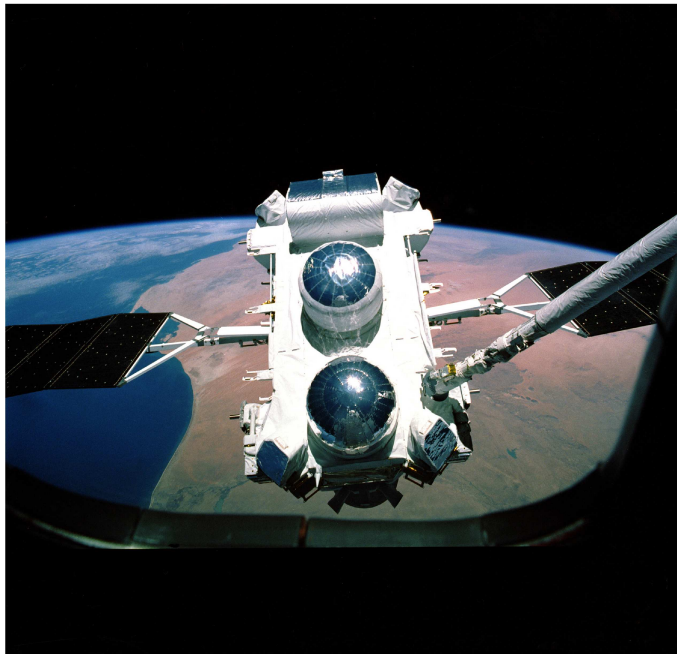

Figure 2.4: Deployment of Compton Gamma Ray Observatory. Credit: NASA.

These instruments included the Energetic Gamma Ray Experiment Telescope (EGRET) that detected events between 20 MeV and 30 GeV with a positional accuracy of $\sim 1°$. The Imaging Compton Telescope (COMPTEL) covered 1 to 30 MeV with a positional accuracy of $\sim 2°$. Currently, Gamma ray imaging observations of nearby galaxies are restricted due to a small number of recorded events at poor positional accuracy.

The Fermi Gamma ray Space Telescope (hereafter Fermi), formerly called Gamma ray Large Area Space Telescope or GLAST, was launched on June 11th, 2008 into a 560 km altitude orbit. It is detecting radiation between 8 keV and 300 GeV using the primary instrument Large Area Telescope (LAT) and the complementary GLAST Burst Monitor (GBM). The LAT has a large field of view, over 2 steradians

(one-fifth of the entire sky), can measure the locations of bright sources to within 1 arcminute and is sensitive to photons from 30 MeV to greater than 300 GeV. The GBM cover X-rays and Gamma rays between 8 keV to 30 MeV, overlapping with the LATs lower-energies.

2.3.2   X-ray

Hard: 3 < kT < 500 keV; Soft: 0.1<kT<3 keV.

The High Energy Astrophysical Observatory-2 (HEAO-2), later named *Einstein*, was launched into low Earth orbit on November 13th, 1978 and operated until April, 1981. It was the first X-ray mission to use focusing optics with imaging detectors and produce angular resolution of a few arc seconds[3] ($''$) and a field-of-view of tens of arc minutes ($'$).

The Röntgen Observatory Satellite (ROSAT; Trümper 1983) was launched on June 1st, 1990 and is currently non-operational, though still orbiting the Earth. ROSAT Position Sensitive Proportional Counter (PSPC) Soft X-ray images spanning the energy range 0.1-2.4 keV, known as Broadband, and 0.1-0.4 keV, known as Softband will be shown in this atlas. Typically, lower energy X-rays are referred to as 'soft', while high energy X-rays, not surprisingly, are designated 'hard'. ROSAT PSPC images have a minimum angular resolution of 25$''$ (FWHM) over a field of view of 2°. ROSAT High Resolution Imager (HRI) has an angular resolution of ∼5$''$ FWHM and a ∼30$'$ field of view.

Chandra X-ray Observatory (CXO), formerly the Advanced X-ray Astrophysics Facility or AXAF), was the U.S. follow-on to *Einstein*, and was launched on July 23rd, 1999. Chandra was the third of NASA's 'Great Observatories'. Chandra has a highly elliptical orbit, 133,000 by 16,000 km, which puts it above the Van Allen belts for ∼85% of its orbit. CXO carries a set of nested high angular resolution mirrors, two imaging detectors (Advanced CCD Imaging Spectrometer, ACIS and High Resolution Camera, HRC), and two sets of transmission gratings (for spectral observations). Important CXO features are: an order of magnitude improvement in angular resolution (above ROSAT and *Einstein*), good sensitivity from 0.1 to 10 keV, and the capability for high spectral resolution observations over most of this range.

XMM-Newton was launched on December 10th, 1999, into a 48 hour elliptical orbit with an apogee of 114,000 km, and perigee of 7000 km. It has a spectral range of 0.1 - 12.0 keV (120 - 1 Å), and its primary imager is the European Photon Imaging Cameras (EPIC).

2.3.3   Extreme Ultraviolet

Extreme (EUV): 100-912Å.

The Extreme Ultraviolet Explorer (EUVE) was launched on June 7th, 1992 and re-entered on January 30th, 2002. EUVE and ROSAT Wide Field Camera (WFC) both had Extreme UV (EUV) survey imaging capabilities. However they do not

---

[3]Seconds of arc are denoted as $''$; minutes of arc as $'$; degrees as °. See Table 7, page 279.
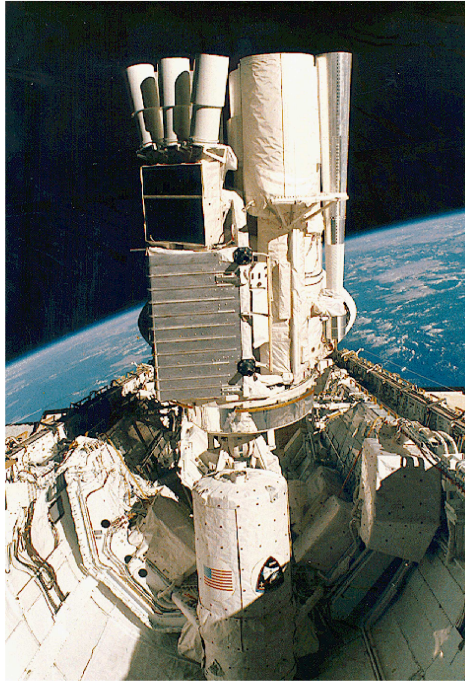
Figure 2.5: *Astro-1* instruments in the Space Shuttle Bay. UIT is the large cylinder blanketed with thermal insulation. Credit: STScI and NASA.

possess the sensitivity nor angular resolution to provide images of galaxies for this atlas. They have been successfully used to produce catalogues of bright sources both of Galactic and extragalactic origin.

2.3.4 Far- and Mid-Ultraviolet

Far-UV: 912-2000Å **; Mid-UV: 2000-3300**Å.

The Ultraviolet Imaging Telescope (UIT; Stecher *et al.* 1992; Figure 2.5) was flown aboard the Space Shuttle *Astro-1* mission (from December 2-11, 1990) and *Astro-2* mission (from March 2-18, 1995). UIT was a 38 cm telescope allowing imaging with a $40'$ field of view. Most images were made with either a broadband Mid-UV (central wavelength $\lambda_c \sim$2000-3000Å) or Far-UV ($\lambda_c \sim$1500-1700Å) filter. The filters used in atlas images are Mid-UV A1 and A5 ($\lambda_c \sim$2800Å and $\sim$2500Å respectively) and Far-UV B1 and B5 ($\lambda_c \sim$1500Å and $\sim$1600Å respectively).

The Swift telescope was launched into a low-Earth orbit on November 20th, 2004. It has a UV/Optical Telescope (UVOT) with wavelength coverage from 170 - 650 nm. Its prime mission is to detect Gamma Ray Bursts (GRBs).

The Galaxy Evolution Explorer (GALEX) was launched on April 28th, 2003. It is a 50 cm Ritchey-Chretien telescope with Far-UV (FUV: 1400-1700Å) and Mid-UV (NUV: 1800-2750Å) imaging capability.

Ultraviolet (Far- and Mid-) observations have been be carried out with Hubble Space Telescope (HST), that was launched on April 24th, 1990 into a near circular low (560 km) Earth orbit. HST (Figure 2.6) was the first of NASA's 'Great Observa-
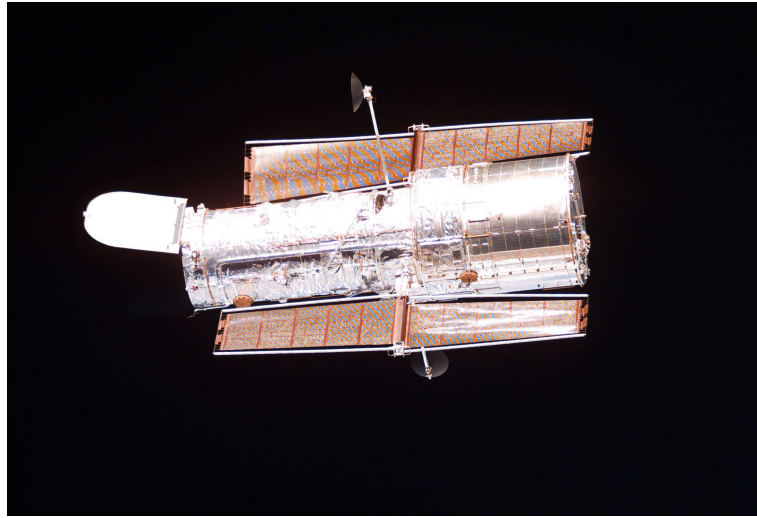
Figure 2.6: Hubble Space Telescope in orbit during the first servicing mission in 1993. Credit: NASA.

tories'. The HST Faint Object Camera (FOC; Paresce 1990) used F175W, F220W and F275W broadband filters with effective wavelengths (λ_{eff}) of $\sim$1900Å, $\sim$2300Å and $\sim$2800Å respectively with bandwidths ($\Delta\lambda$) of $\sim$500Å. FOC was removed from HST in March, 2002.

2.3.5   Optical

3300 to 8000Å.

Optical images in the atlas have been taken with a variety of ground-based telescopes as listed in Appendix B (page 268). The instruments used were typically prime focus cameras with Charge Coupled Devices (CCDs) as detectors. Hubble Space Telescope Wide Field Planetary Camera (WFPC; Westphal 1982), Wide Field Planetary Camera-2 (WFPC2; Holtzman *et al.* 1995), Advanced Camera for Surveys (ACS; Ford et al. 1998) and Wide Field Camera 3 (WFC3) CCD images are also presented.

Standard broadband ($\Delta\lambda > 650$ Å) optical filters include U ($\lambda_{\mathrm{c}} \sim$3600Å), B ($\lambda_{\mathrm{c}} \sim$4400Å), V ($\lambda_{\mathrm{c}} \sim$5500Å), R ($\lambda_{\mathrm{c}} \sim$6500Å) and I ($\lambda_{\mathrm{c}} \sim$8200Å). Narrowband ($\Delta\lambda < 100$ Å) filters are also used to isolate individual emission lines such as Hα (6563Å) and [N II] (6548,6583Å).

2.3.6   Near-Infrared

Near-IR: 0.8-7 μ**m**.

Near-IR images have been taken with the Steward Observatory 2.3 m and 1.6 m, University of Hawaii 88 inch and the KPNO 1.3 m telescopes. Standard Near-IR filters include J ($\lambda_{\mathrm{c}} \sim$1.25 μm), H ($\lambda_{\mathrm{c}} \sim$1.65 μm), K ($\lambda_{\mathrm{c}} \sim$2.2 μm), L ($\lambda_{\mathrm{c}} \sim$3.5 μm) and M ($\lambda_{\mathrm{c}} \sim$5 μm). Mosaiced three-color Near-IR images from the Two Micron All Sky Survey (2MASS) are also shown. 2MASS used two 1.3 m telescopes, one at

Mt. Hopkins, Arizona, and one at CTIO, Chile. Each telescope was equipped with a three-channel camera, each channel consisting of a 256 × 256 array of HgCdTe detectors, capable of observing the sky simultaneously at J, H, and K$_s$ (2.17 μm).

2.3.7 Mid- and Far-Infrared

Mid-IR: 7-25 μm; Far-IR: 25-300 μm.

The Infrared Astronomical Satellite (IRAS; Neugebauer *et al.* 1984) was launched on January 25th, 1983 into a 900 km altitude orbit. It produced an all-sky survey covering 96% of the sky at wavelengths of 12, 25, 60 and 100 μm. IRAS had a 0.57 m diameter primary mirror and the telescope was mounted in a liquid helium cooled cryostat. The mirrors were made of beryllium and cooled to approximately 4 K. On November 22nd, 1983 the survey finished due to the depletion of on-board liquid helium.

The Infrared Space Observatory (ISO; Kessler *et al.* 1996) was launched on November 17th, 1995 and ceased observation in April 1998. ISO operated from 2.5 to 240 μm. It had a 60 cm diameter primary mirror and several instruments including ISOPHOT (Lemke *et al.* 1996) that could perform imaging as well as polarimetry[4].

The Spitzer Space Telescope (SST; formerly SIRTF, the Space Infrared Telescope Facility; Werner *et al.* 2004) was launched on August 25th, 2003 and is the fourth and final telescope in NASA's family of 'Great Observatories'. SST is in an Earth trailing heliocentric orbit and moves away from Earth at ∼0.1 AU[5] per year. SST has an 85 cm diameter mirror and three cryogenically cooled science instruments capable of performing imaging and spectroscopy between 3.6 to 160 μm. Wide field, broadband imaging is done by the Infrared Array Camera (IRAC) and the Multiband Imaging Photometer for Spitzer (MIPS).

2.3.8 Submillimeter and Radio

Submillimeter: 300 μm - 1mm; Radio: 1mm and longer wavelengths.

The 15 m diameter, alt-azimuth (alt-az) mounted James Clerk Maxwell Telescope (JCMT; Figure 2.7) on Mauna Kea, Hawaii, operates specifically in the mm (radio) and submillimeter regions. Since May 1997 the Submillimeter Common-User Bolometer Array (SCUBA) instrument on JCMT has produced observations between 350 and 850 μm. A new generation SCUBA-2 is expected to begin operation post-2009.

The Owens Valley Radio Observatory (OVRO), located near Bishop, CA, U.S.A., has a Millimeter Wavelength Array comprising of six 10.4 m telescopes with Half Power Beam Widths (HPBW; a spatial resolution measure similar to FWHM) equal to 65 ″. The array is used for aperture synthesis mapping of millimeter line

---

[4]Electromagnetic waves may travel in a preferred plane - unpolarized light does not have a preferred plane of vibration. Polarimetry is the measure of a preferred plane of propagation and the amount is called the polarization and can be between 0 and 100%.

[5]Astronomical Unit, or AU, is the average distance between the Earth and Sun.
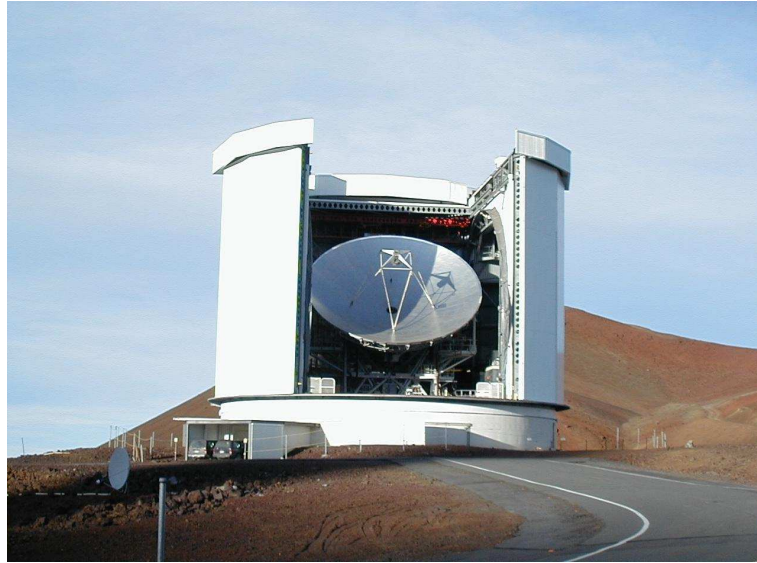
Figure 2.7: A rare view of the James Clerk Maxwell Telescope after the telescope membrane had been removed in preparation for removing the Secondary Mirror Unit. Credit: James Clerk Maxwell Telescope, Mauna Kea Observatory, Hawaii.

and continuum emission in the 2.7 and 1.3 mm windows. The Columbia Southern Millimeter-Wave Telescope is a 1.2 m diameter Cassegrain telescope located at CTIO, Chile and is described in Bronfman *et al.* (1988).

The Very Large Array (VLA), a 27-antenna radio telescope array is located in Socorro, New Mexico, U.S.A. The telescope consists of 25 m diameter parabolic dishes, which can be placed along a Y-shaped pattern with each of the arms being 20 km long. The VLA can observe radiation between 1.3 and 22 cm and achieve an angular resolution similar to a telescope of size 27 km in diameter via aperture synthesis.

The Westerbork Synthesis Radio Telescope (WSRT) is a 3 km long array of fourteen 25 m antennas, located near Hooghalen, Netherlands. The Jodrell Bank 76 m radio telescope (now known as the Lovell Telescope) is an alt-az mounted telescope in Cheshire, England. The Effelsberg (near Bonn, Germany) 100 m radio telescope was the world's largest moveable radio telescope until August 2000 when the 100 m × 110 m Robert C. Byrd Green Bank Telescope in Virginia saw 'first light'.

The Australia Telescope Compact Array (ATCA) in Narrabri, New South Wales consists of six 22 m antennas (five antenna are located on a 3 km E/W railway and one a further 3 km to the west). The Parkes (New South Wales, Australia) radio telescope (Figure 2.8) is a single 64 m diameter antenna on an alt-az mounting that operates between wavelengths of 1 to 70 cm (21 to 0.5 GHz).

Very Long Baseline Interferometry (VLBI) is conducted by many radio antennas separated by large distances to achieve very high angular resolution. The signals from astronomical sources are recorded on large capacity disk drives along with accurate timing information (usually via a highly stable hydrogen maser clock) and processed by a signal correlator. The correlator removes known geometric delay and
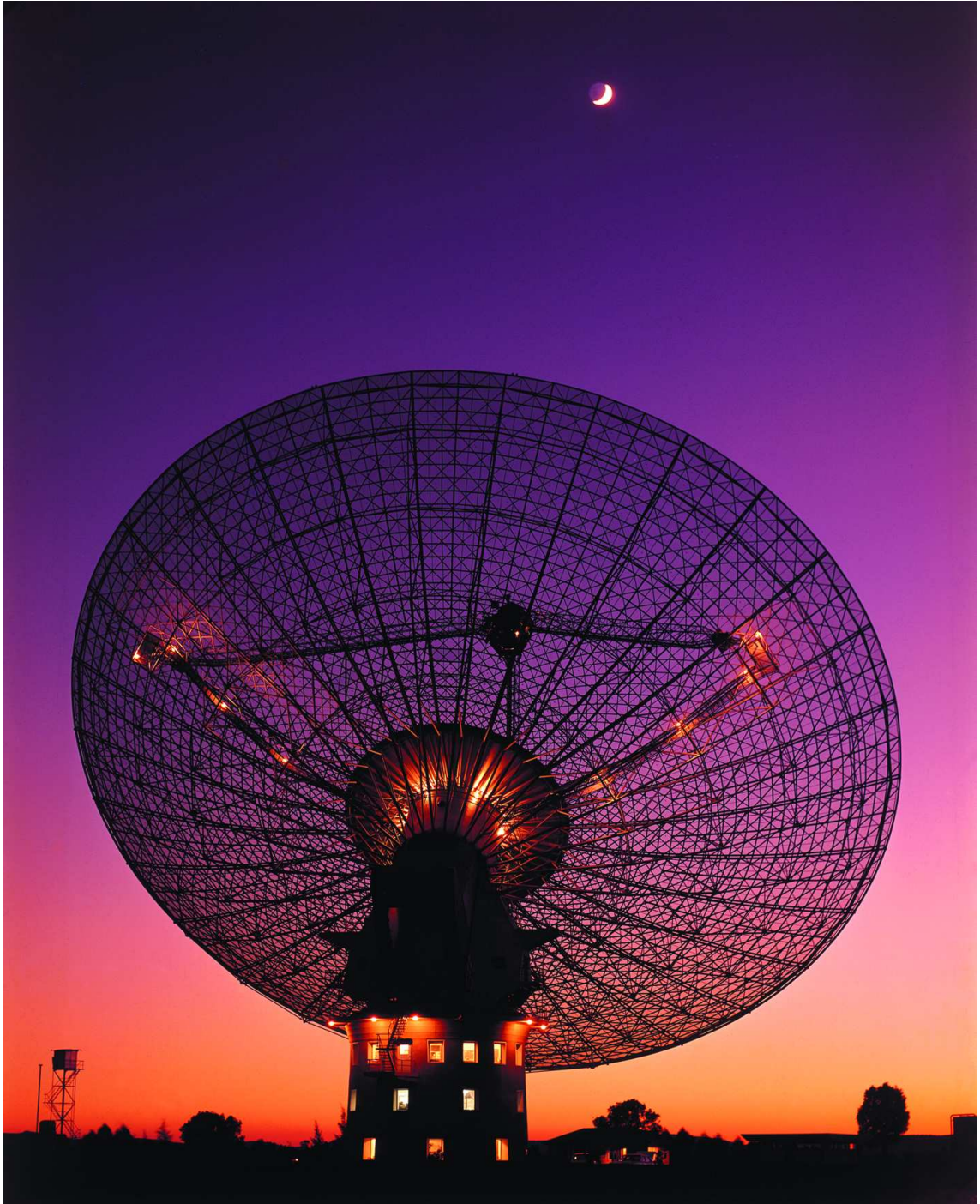
Figure 2.8: Parkes 64 m radio telescope. ©Seth Shostak.

Doppler shift due to the Earth-based motion of the antennas. The Southern Hemisphere VLBI Experiment (SHEVE) array was an ad hoc array of radio telescopes in the Southern Hemisphere (mainly in Australia with occasional contributions from Sth. Africa). The Australia Telescope National Facility (ATNF) now operates the Long Baseline Array (LBA) consisting of ATCA, Mopra, and Parkes. There is an Australian VLBI National Facility, comprising the LBA plus University of Tasmania antennas at Hobart and Ceduna, and the Tidbinbilla antenna.

2.4   Astronomical Sources of Radiation

The entire electromagnetic spectrum (Figure 1.6) stretches more than 15 orders of magnitude (a factor of 10^{15}) from short wavelength ($\sim 10^{-10}$ cm) high frequency Gamma rays through X-rays, Ultraviolet, Optical, Infrared, Submillimeter to the longest wavelengths ($\sim 10^5$ cm) lowest frequencies of the Radio region.

The observational limits of electromagnetic radiation from astronomical objects are not well established. At high energy, short wavelengths, TeV (where T is Tera or 10^{12}) Gamma rays have been detected from some AGN. In comparison the highest energy cosmic ray particles (typically protons), above 10^{19} eV (or 10^7 TeV), arrive at a rate of about one particle per square kilometer per year. Low to medium energy cosmic rays, up to energies of about 10^{18} eV, probably originate in the Galaxy via interactions with magnetic fields. Higher energy cosmic rays are most likely extragalactic in origin, possibly in AGN or supernovae.

At low energy, long wavelengths, radio radiation has been detected at wavelengths of about 1.2 km (frequency 0.25 MHz; Novaco and Brown 1978). The long wavelength limit of a few km is set by absorption in the interplanetary and interstellar media.

What types of objects emit radiation and in what region of the electromagnetic spectrum is it detected? Table 3 (page 57) describes the main spectral regions and lists astronomical sources of emission and absorption in each region.

Table 3: Astronomical Sources of Emission and Absorption

Spectral Regions	Emission: Stellar	Emission: Interstellar	Absorbers
kT > 500 keV (**Gamma ray**)	Pulsars, Bursts?	ISM scattered	
3 keV <kT<500 keV (**Hard X-ray**)	X-ray Binaries; AGN?	Ultra-hot ISM, ICM	
0.1<kT<3 keV (**Soft X-ray**)	Main Seq. Stars; Evolved SNe	Hot ISM, ICM; SNRs	Dust
100-912Å (**EUV**)	O Stars; Pop. II Evolved; Accreting Binary Stars	Hot ISM, SNRs	Dust; H, He
912-2000Å (**Far-UV**)	Pop. I, M>5 $M_\odot$ Pop. II Evolved	H II, Lyman Alpha, Planetary Nebulae	Dust, Metals H_2, Lyman Alpha
2000-3300Å (**Mid-UV**)	Pop. I, M>1.5 $M_\odot$ Pop. II, Horiz. Branch	–	Dust, Metals Ionized species
3300-8000Å (**Optical**)	Pop. I Evolved (BA, M); M> 1 $M_\odot$ Main Seq., Pop. II Main Seq.; Evolved (K,M): Horiz. Branch	H II, H-Balmer; Forbidden Metal Emission Lines, [O],[S],[N],[Ne]	Dust, Metals
0.8-7 μm (**Near-IR**)	Evolved Red Giants, Supergiants, AGB Stars; Protostars	H II; Hot Dust, PAHs; H_2 emission	Dust; PAHs
7-25 μm (**Mid-IR**)	Hot Circumstellar Dust, OH/IR stars; Protostars	H II; PAHs, Small Grains	Dust
25-300 μm (**Far-IR**)	Carbon Stars, Protostars	H II; Dust	Dust
300 μm -1 mm (**Sub mm**)	–	Dust; Therm. Brems. Molecular ISM; Non-Thermal	–
1mm – (**Radio**)	–	Non-Thermal, Therm. Brems.; Molecular ISM (CO, etc.) Masers Neutral ISM (H I) H II	–

Notes to Table 3

- This table is adapted from Table 1 of Gallagher and Fabbiano (1990). With kind permission of Springer Science and Business Media.

- Units/Symbols: Gamma rays are typically described in units of T(era)eV, G(iga)eV, M(ega)eV. kT is a symbol for energy, typically used in X-ray astronomy, where k (Boltzmann's constant) = 1.38 x 10^{-16} erg/K; X-rays in k(ilo)eV; EUV, Far-UV, Mid-UV and Optical in Å or nm; Near-IR, Mid-IR, Far-IR in μm; Sub mm in μm, mm and GHz; Radio in cm, m, MHz and GHz.

- Whilst CO observations are usually regarded as 'mm' observations, to be consistent with the above Spectral Region divisions CO observations at wavelengths longer than 1 mm will be considered as radio observations.

- **Pop. I** - Population I are stars and clusters that are relatively young, and are typically found in the Galactic disk region. Formed from enriched material

from previous stellar generations they tend to have high metallicities.[6]

- **Pop. II** - Population II are stars and Globular clusters that are relatively old, and are typically found in the spherical halo of the Galaxy. They have low metallicities, being formed earlier than Pop. I from less enriched material.

- **X-ray Binaries** - Binary star systems in which one component is a degenerate star (e.g. white dwarf, neutron star or black hole). X-rays are emitted from either a gaseous accretion disk in low-mass X-ray binaries (LMXBs; when the two stars are of similar masses an accretion disk forms around the degenerate star) or from an extended envelope in high-mass X-ray binaries (HMXBs; when one component is $\sim$10-20 $M_\odot$ and gas flows directly onto the degenerate component).

- **PAHs** - Polycyclic Aromatic Hydrocarbons, a component of interstellar dust made up of small dust grains (e.g. silicates) and soot-like material. 'Hydrocarbon' refers to a composition of C and H atoms. 'Polycyclic' indicates the molecules have multiple loops of C atoms. 'Aromatic' refers to the kinds of bonds that exist between the C atoms. PAHs are formed during incomplete combustion of organic (i.e. carbon-based) material. Observations of the 'Red Rectangle' (HD 44179) nebula by Vijh, Witt, and Gordon (2004) showed blue luminescence at $\lambda < 5000$ Å. The authors attribute this to fluorescence by PAH molecules with three to four aromatic rings such as anthracene ($C_{14}H_{10}$) and pyrene ($C_{16}H_{10}$). However Nayfeh, Habbal and Rao (2005) also suggest that ultrasmall silicon nanoparticles of 1 nm in diameter could be the source of emission.

- **SNRs** - A supernova remnant (SNR) is the remains of a supernova explosion. Massive stars end their lives by imploding, and the outer layers of gas are blown outwards at velocities up to 15,000 km s^{-1}.

You know what finally happened. ..., I concluded that we had to distinguish at least two H-R diagrams - one the normal diagram that we had known well for some time, the other, the globular-cluster diagram.

Walter Baade

---

[6]The metallicity or metal abundance measures the amount of elements other than hydrogen or helium in a star or gas. This is typically expressed for a star as relative to the Sun as [Fe/H] = $\log_{10}\left(\frac{N_{Fe}}{N_H}\right)_{star}$ - $\log_{10}\left(\frac{N_{Fe}}{N_H}\right)_\odot$ where N_{Fe} and N_H are the number of iron and hydrogen atoms per unit volume respectively.

2.5 Origin of Astronomical Radiation

In the following section the main sources of astronomical radiation will be described.

2.5.1 Gamma rays

kT > 500 keV.

Observations of Gamma rays are the most difficult of all multiwavelength detections and accurate identification of their origin is still debatable in some cases. The detection of faint extragalactic sources is difficult because the photons have to be detected against a high background of cosmic rays[7]. The angular resolution of Gamma ray telescopes is presently quite low, and optical identification of Gamma ray sources (especially when associated with faint optical sources) has proven very difficult.

However Porter *et al.* (2009) show for the first time an external galaxy resolved in Gamma rays. The Fermi LAT has resolved the Gamma ray emission from the LMC. The LMC is observed with an integration time of 211.7 days with energies between 200 MeV and 100 GeV and the Gamma ray signal is dominated by emission from the star forming region 30 Doradus. The overall Gamma ray emission does not seem to correlate with the molecular gas distribution but better matches the atomic H I distribution.

Detections in other wavelengths can help pinpoint the origin of Gamma ray sources. For example the Vela and Crab pulsars emit pulsed radiation in both the Gamma ray and radio regions with the same periodicity, allowing certain Gamma ray source identification. Pulsars can produce Gamma ray emission if material falls onto their surface and is heated to temperatures of a few 10^6 K.

Strong Gamma ray sources in our Galaxy include the Galactic plane, and several nearby pulsars (Figure 1.16 and Figure 3.5). The emission from the plane can be accounted for by inelastic collisions between high energy cosmic rays, probably protons, and the nuclei of atoms and ions in interstellar gas. Such collisions result in the production of π mesons[8] which decay to two 70 MeV Gamma rays.

This decay mechanism probably explains the high energy (>100 MeV) events, whilst at lower energies Bremsstrahlung radiation (see below) could greatly contribute (see Longair 1997 for a detailed discussion).

The high X-ray luminosities of AGN strongly suggest that they should also be sources of Gamma rays. This is now confirmed by observations. COMPTEL observations suggest the existence of 'MeV quasars' that may contribute substantially to an MeV 'bump' in the Gamma ray background[9] spectrum. EGRET observations have discovered bright, variable Gamma ray emission from Blazars. These sources

---

[7]Energetic particles travelling close to the speed of light. Primary cosmic rays originate beyond the Earth's atmosphere. Secondary cosmic rays are produced when primary cosmic rays collide with atmospheric atomic nuclei, and are detected as air showers.

[8]The strong nuclear force binds together protons and neutrons, involving the exchange of short-lived particles called mesons.

[9]The Gamma ray background is the integrated emission from sources in the Gamma ray region that are not resolved. These unresolved sources could be very faint or diffuse or both.

are identified with highly polarized OVVs (Optically Violent Variables) in which relativistic beaming is most likely occurring. Even higher energy emission has been detected from some AGN. Gamma rays exceeding 5 ±1.5 TeV have been detected from Markarian[10] 421 (a BL Lac object; Krennrich *et al.* 1997) using the Whipple Observatory's 10 m telescope in Arizona.

The Gamma ray ultra high energy emission is related to a jet or beamed energy originating in a putative SMBH and surrounding accretion disk. Gamma rays are produced by the beam of relativistic particles which is ejected and collimated by strong magnetic fields in the inner accretion disk region. The highest energy emission is seen in such objects when the jets are viewed end-on, which is occurring in Blazars like Markarian 421.

Whilst Gamma rays are absorbed by our atmosphere, Very-High-Energy (VHE) Gamma rays can be detected from the ground via the secondary radiation they produce when they strike components of the Earth's atmosphere. This radiation is produced as a brief flash of light that only lasts for a few billionths of a second. This light can be detected with large optical light collectors equipped with photomultiplier tubes as on the Whipple Observatory 10 m telescope.

Gamma ray astronomy is now heavily focussed on Gamma ray Bursts (GRBs; Fishman 1995; Paczyński 1995). These intense outbursts vary in duration from a few milliseconds to a few tens of seconds. GRBs are now known to be extragalactic in nature and appear to occur in the outskirts of distant galaxies. Gamma Ray Bursts are discussed in more detail in Section 2.9.4.

2.5.2   X-rays

Hard: 3 keV $<$kT$<$500 keV; Soft: 0.1$<$kT$<$3 keV.

The Soft X-ray region (0.1$<$kT$<$3 keV) can also be subdivided into smaller energy regions (e.g. see the 0.2-1.5 keV CXO observation of the NGC 253 atlas images, beginning page 197). X-rays originate from a variety of physical processes.

First, gas that is hotter than 10^6 K is fully ionized (i.e. all electrons are dissociated from their atoms). The electrons are accelerated due to proton encounters and radiate energy via the Bremsstrahlung process. This radiation is emitted by hot gas associated with SNRs and by hot gas that surrounds many elliptical galaxies and galaxy clusters.

Bremsstrahlung, or Breaking Radiation, (Figure 2.9) occurs when charged particles, typically electrons, are decelerated over a very short distance. At temperatures higher than 10^5 K gas consists of positive ions and electrons. In Bremsstrahlung, a continuous spectrum with a characteristic profile and energy cutoff (wavelength minimum) is produced

$$I(E, T) = C \, G(E, T) \, Z^2 \, n_e \, n_i (kT)^{-1/2} \, e^{-E/kT}$$

---

[10]Markarian galaxies are galaxies catalogued by the astronomer B.E. Markarian based on their strong continuum emission in the UV.

where I(E,T) is the intensity (a function of energy, E and temperature T), C is a constant, G is the 'Gaunt factor' (a slowly varying function), Z is the charge of the positive ion, n_e is the electron density, n_i is the positive ion density.

This emission is characterized by the temperature of the gas. The higher the temperature, the faster the electrons, and the higher the photon energy of the radiation. Bremsstrahlung radiation is also known by astronomers as free-free emission - since the electron starts free and ends free.
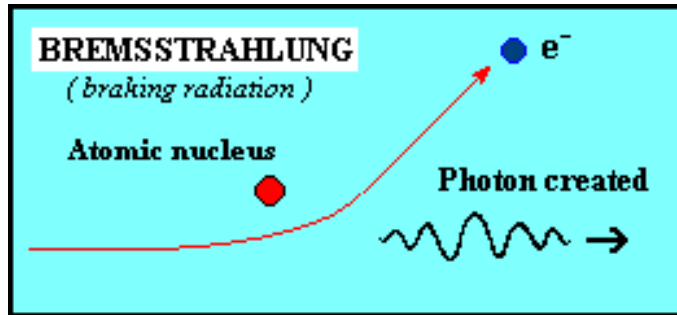

Figure 2.9: Bremsstrahlung radiation. Credit: XXX.

Second, electrons spiraling in a magnetic field will emit synchrotron radiation. Synchrotron X-ray emission (Figure 1.14) requires very energetic, high velocity electrons in strong magnetic fields. An example of this process is found in the SNR Crab Nebula. The intensity is of the form

$$I(E) = C\ E^{-\alpha}$$

where intensity I is only a function of energy, E, C is a constant, and α is the spectral 'index'. Larger values of α correspond to a higher proportion of lower energies emitted.

Third, X-ray emission can be blackbody radiation. In this case, an object is called a 'blackbody' if its surface re-emits all radiation that it absorbs. The continuum emission radiated is described by only one parameter, the objects temperature. X-ray blackbody radiation is emitted from very hot objects with surface temperatures $> 10^6$ K, such as neutron stars. The intensity is given by the Planck law

$$I(E, T) = 2\ E^3\ \left[h^2c^2(e^{E/kT} - 1)\right]^{-1}$$

where intensity is a function of energy, E and temperature T, h is Planck's constant, and c is the speed of light.

Observations of the Galaxy and Local Group members suggest that much of the total X-ray emission from spiral galaxies originates from discrete sources such as accreting binaries and SNRs. Diffuse emission has been detected in many spirals and originates from hot gas energized by shocks or outflows (e.g. caused by supernovae) in their disks. Hot, 10^{6-7} K, gaseous halos around elliptical galaxies and clusters of galaxies were discovered by *Einstein*. These originate from accumulated ejected gas (mass loss) from the evolved stellar population, as confirmed by the enriched metal
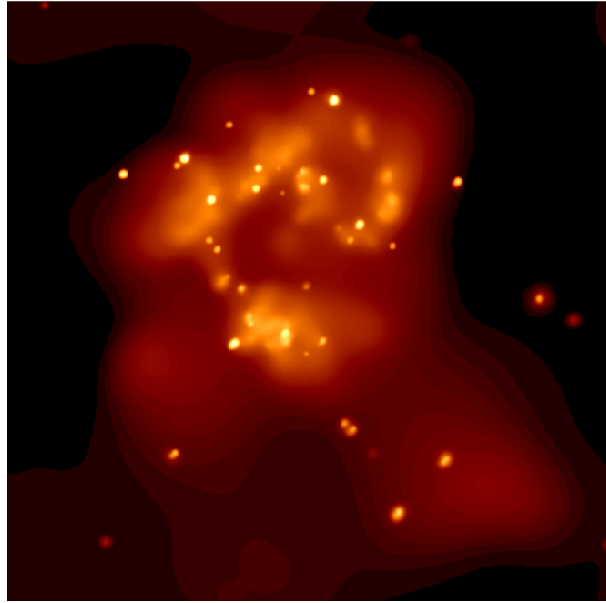
Figure 2.10: CXO X-ray image of the merging galaxies NGC 4038/9. The image is 4′ on a side. Credit: NASA/SAO/CXC/G. Fabbiano.

content of the gas. Characteristics of elliptical galaxy X-ray emission also suggest an underlying discrete source component, most likely from accreting binaries.

Figure 2.10 shows a CXO image of the central regions of the merging galaxies NGC 4038/9. The bright point-like sources are binary systems containing either neutron stars or black holes which are accreting gas from donor stars. The X-ray emission originates from accretion disks around these degenerate stars. Other more extended X-ray emission is associated with hot gas energized by numerous supernova explosions, stimulated by the merger process.

X-ray emission is also very strong in AGN and originates from a variety of sources. A component can be linked with frequently observed beamed radio and Gamma ray emission. X-ray emission with low (<1 keV) energies can be variable on timescales as short as several hours. This emission probably originates close to the active core of the AGN, most likely in the inner region of an accretion disk. Higher energy X-ray emission in AGN is caused by inverse Compton scattering (Figure 2.11) which is an exchange of energy between electrons and photons in dense gas although for quasars this component is weak or absent.
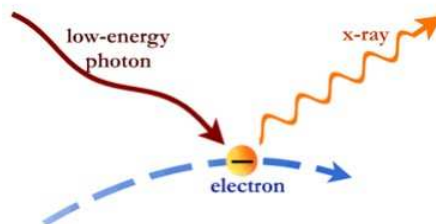

Figure 2.11: Inverse Compton Scattering. Credit: XXX

An important emission line is seen in many AGN at 6.4 keV due to X-ray fluorescence[11] from iron at temperatures of several million K. Photons striking the accretion disk of the AGN are absorbed by electrons of iron which then de-excite by emitting a photon of energy 6.4 keV. This Fe Kα line is an important diagnostic of the kinematics of accretion disk gas near the central black hole. The ASCA satellite made a deep exposure of the Seyfert 1 galaxy MCG-6-30-15 (Tanaka *et al.* 1995) showing a broad Fe Kα line that would infer relativistic gas speeds of $\sim$100,000 km s^{-1} or 0.3c. The line profile is sometimes asymmetric consistent with relativistic effects and provides compelling evidence for not only the existence of SMBHs but also black hole spin (Miller 2007).

2.5.3 Ultraviolet

Extreme (EUV): 100-912Å ; Far-UV: 912-2000Å ; Mid-UV: 2000-3300Å.

The EUV region is dominated by emission from (in order of decreasing number of detections in the 2nd EUVE Source Catalog) late-type stars (F to M spectral classes), hot white dwarf stars, early-type stars (A, B spectral classes), cataclysmic[12] variables and AGN (mainly Seyferts and BL Lacs). EUV observations (i.e. ROSAT WFC and EUVE) consist of medium angular resolution surveys that generally detect objects in the Galaxy.

Based on the soft X-ray properties of some AGNs, many active galaxies were predicted to be detected in the Ultraviolet. In fact WFC detected 7 AGN (3 were Blazars) whilst Marshall, Fruscione and Carone (1995) detected 13 AGN (7 Seyferts, 5 BL Lacs and 1 quasar) in the EUVE all-sky survey. By searching the EUVE archive for sources near known extragalactic X-ray sources, Fruscione (1996) finds that 20 X-ray galaxies (12 Seyferts, 1 LINER, 6 Blazars, 1 quasar) are strong EUVE sources. High angular resolution EUV imaging of nearby galaxies does not exist.

The Ultraviolet is very rich in spectral lines. These atomic and molecular lines are useful for deriving important astrophysical information. Hot (10,000 - 40,000 K) stars emit a large fraction of their radiation in the Ultraviolet. Imaging studies in the Far-UV and Mid-UV detect hot stars associated with star forming H II regions and young star clusters in spiral galaxies. Spectral studies of O VI (doublet at 1032Å, 1038Å) absorption in hot gas clouds by the FUSE satellite (launched on June 24th, 1999 and operational until October 18th, 2007) has given important diagnostic information about the intergalactic medium.

Far-UV and Mid-UV images of ellipticals (e.g. M 32 the satellite galaxy of NGC 224/M 31; Figure 2.12) and spiral galaxy bulges has shown that the unexpected UV excess (first observed by the OAO series of satellites in the 1970s) is not caused by recent massive star formation, but probably by low-mass, post-giant branch stars.

The emission of quasars peak around the UV region - 'the big blue bump' is the well-known feature with a peak energy around the Lyman limit of 1216Å (Risaliti

---

[11]Certain substances can absorb radiation at one wavelength and re-emit it. Usually the fluorescent-based emission is at a larger wavelength and has less energy.

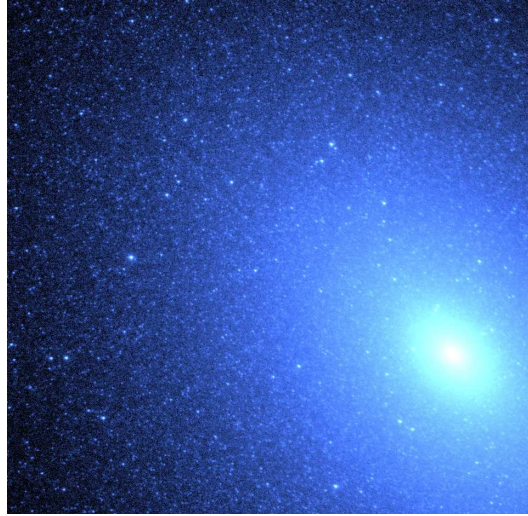[12]A rapid or dramatic brightening due to an explosive event - e.g. a novae, flare.

Figure 2.12: UV image of M 32 by STIS on HST. The nucleus is at lower, right. The UV excess seen in ellipticals and bulges originates in the observed population of old, but hot, helium-burning stars. Credit: NASA and T. M. Brown, C. W. Bowers, R. A. Kimble, A. V. Sweigart (NASA Goddard Space Flight Center) and H. C. Ferguson (STScI).

and Elvis 2004). This peak is best described by thermal emission from accretion disk gas displaying a wide range of temperatures.

UV radiation is greatly attenuated by dust grains. These grains are very good absorbers of photons which have wavelengths equal to or smaller than the size of the grain. Many grains have characteristic sizes of 100 nm or more which means that interstellar dust absorbs UV radiation very efficiently.

2.5.4   Optical

3300 to 8000Å.

In normal galaxies optical emission is dominated by radiation from the photospheres of stars. Stars radiate in a similar fashion to a blackbody, with surface temperatures ranging from 3,000 K (M dwarfs) to 40,000 K (O type). Our Sun is a G dwarf type spectral class with a surface temperature of 5,800 K. Peak emission from stars with temperatures of 8,700 K and 3,625 K occurs at the limits of the optical region, 3300 and 8000Å, respectively. Wien's law for a blackbody allows us to calculate the wavelength of maximum emission

$$\lambda_{\mathrm{max}} = \frac{0.0029 \, \mathrm{K \, m}}{\mathrm{T}}$$

where λ_{max} is the wavelength of maximum emission in meters and T is the temperature of the object in K. The total amount of energy radiated by a blackbody is given by the Stefan-Boltzmann law

$$\mathrm{F} = \sigma \, \mathrm{T}^4$$

where F is the energy flux in joules m^{-2} s^{-1}, σ is a constant (5.67 x 10^{-8} W m^{-2} K^{-4}), and T is the temperature in K. Based on these laws there are two key things to remember. Firstly, that temperature is inversely related to λ_{max}, hence if you double the surface temperature of a star, λ_{max} will halve. Secondly, the same temperature increase will increase the energy flux by a factor of 2^4 or 16.

Filters can be used to isolate a narrow range of optical emission. For example, observing a spiral arm, blue light (e.g. using a 'B' filter with $\lambda_c \sim$4500Å) images will preferentially record radiation from young, hot stars whilst red light (R or I with λ_c > 6000Å) images will be dominated by radiation from cooler, more evolved stars. Figure 2.13 shows dwarf star spectra (Jacoby, Hunter and Christian 1984) from O to M spectral types. Notice how the energy maxima increases to longer wavelengths in the progression from O (hot stars) to M (cooler) types.
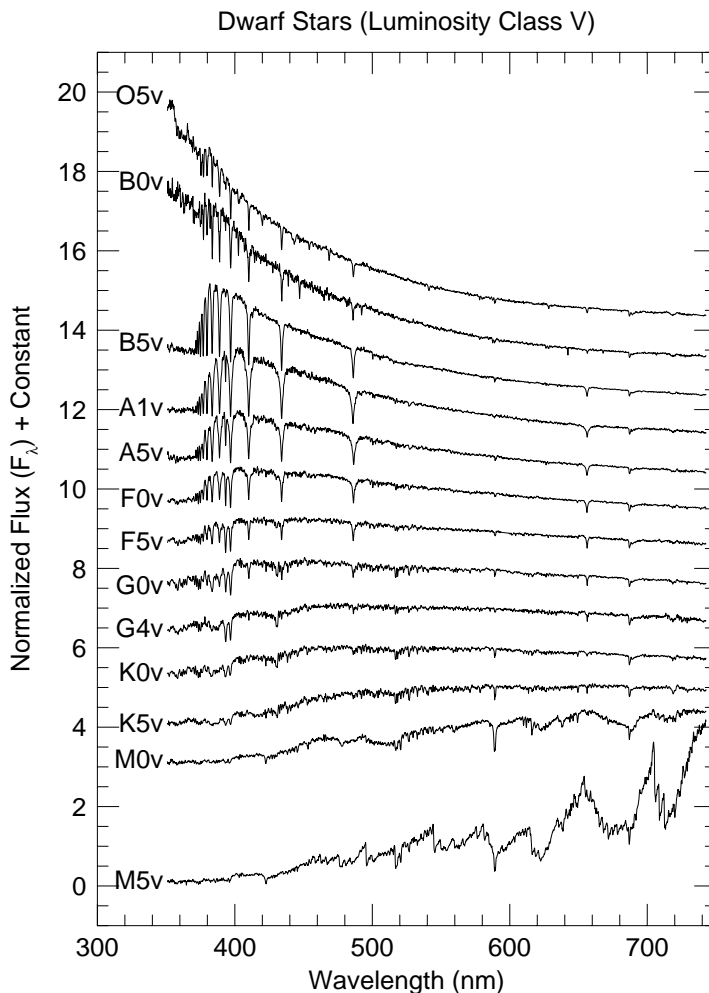

Figure 2.13: Optical Spectra of Dwarf Stars from Jacoby, Hunter and Christian (1984) showing O to M spectral types. Credit: Supplied by R. Pogge. Figure courtesy of G. Jacoby/NOAO/AURA/NSF. Reproduced by permission of the AAS.

Radiation from warm, 10^4 K gas, typically found in and near star forming regions

(also called H II regions), can also be detected in the optical region. This element of the ISM is usually detected by observing the recombination[13] emission line of singly ionized hydrogen (usually denoted by Hα) at 6563Å. An example of this emission in the LMC is shown in Figure 2.14.
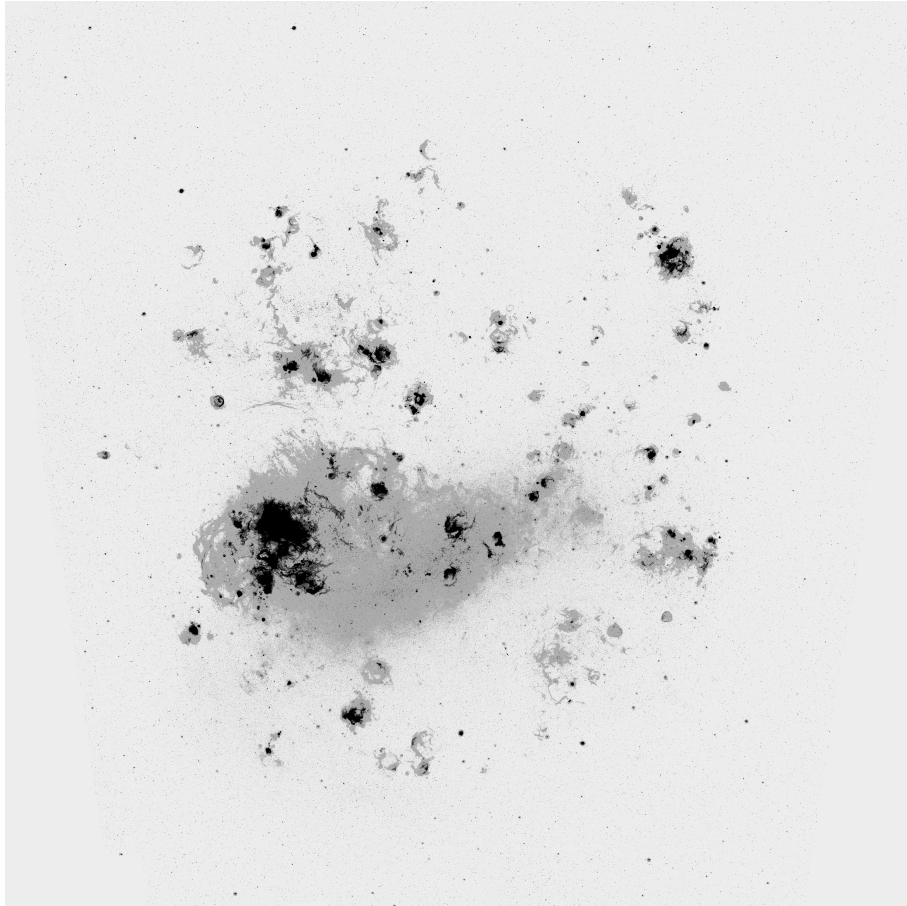

Figure 2.14: Hα image of the Large Magellanic Cloud. Credit: C. Smith, S. Points, the MCELS Team and NOAO/AURA/NSF.

Other important diagnostic lines include the hydrogen Balmer series lines Hβ (4861Å) and Hγ (4340Å), and He I (5876Å) and He II (4686Å). Forbidden lines of ions such as the oxygen doublet [O III][14] (4959, 5007Å), (Figure 2.15), the nitrogen doublet [N II] (6548, 6583Å; surrounding the Hα line), the oxygen doublet [O II] (3726, 3729Å) and the Sulphur doublet [S II] (6716, 6731Å) are also seen. H II regions are powered by UV radiation from nearby, hot stars. This radiation is absorbed by the gas and then re-emitted, mainly in the optical and IR regions.

Optical emission can be greatly attenuated by interstellar dust. Light is absorbed and scattered by dust particles or grains, and this attenuation is greater for shorter

---

[13]Recombination occurs when an electron is captured by an ion and energy in the form of photons is emitted corresponding to atomic energy levels.

[14][ ] indicate forbidden lines, where the 'III' notation represents the doubly ionized species; similarly 'II' is singly ionized, etc.
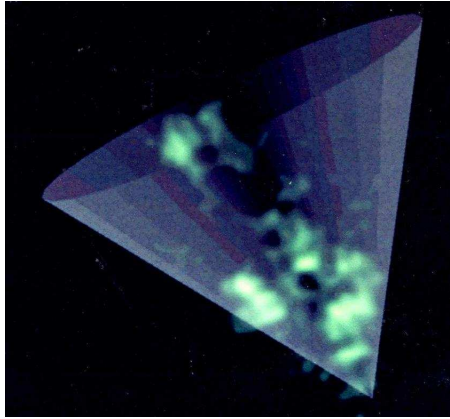
Figure 2.15: Optical [O III] emission depicted as green in the Seyfert 2 galaxy NGC 1068/M 77. The nucleus is at the bottom, right and the cone is an artists impression to guide the eye. The image is $\sim 1.5''$ across. Credit: Faint Object Spectrograph Investigation Definition Team, NASA.

wavelengths. Hence, many B images in the atlas will show dramatic evidence of dust absorption in and near spiral arms, whereas in red images (e.g. R or I) the effect is less pronounced. Absorption and scattering can diminish the light from stars. Taken together astronomers refer to this as extinction. The extinction, A, is the difference between the observed magnitude and the magnitude in the absence of dust. Likewise, the color excess or reddening, E, is the difference between the observed color and the intrinsic color. The most cited extinction is A_V in the optical V, and color excess is E(B-V) where B and V are the standard optical broadband filters

$$\text{E(B} - \text{V)} = \text{(B} - \text{V)}_{\text{intrinsic}} - \text{(B} - \text{V)}_{\text{observed}}$$

Where B and V are the standard optical broadband filters. It is assumed A tends to 0 at very long wavelengths, and

$$\text{A}_{\text{X}} = \text{A}_0 \, \text{f}(\lambda_{\text{X}})$$

where A_0 is a constant and f is a theoretical function. Extinction curves for particular lines of sight can be determined. A_λ has a maximum in the far-UV whilst shorter wavelength X-rays can pass through dust grains, and much longer wavelength radiation refracts around the grains. A significant extinction 'bump' or maxima exists at 217.5 nm which could be caused by graphite or PAHs. Several other features between 3.3 and 12 μm could be related to PAHs as well, as they have wavelengths of vibration modes in C-C and C-H bonds that are common in PAHs. In the Far-IR A_λ decreases with increasing wavelength as λ^{-1} but there is variation in A_λ particularly in the UV for different lines of sight.

The slope of the extinction curve near V in the optical is

$$\frac{\text{A}_{\text{V}}}{\text{A}_{\text{J}}\text{R}_{\text{V}}}$$

where

$$R_V = \frac{A_V}{E(B-V)}$$

Traditionally R_V has been taken to be 3.1 but it can range from $\sim$3 (steeply increasing extinction into the UV) to $\sim$5 (slowly increasing extinction into the UV). E(B-V) is not surprisingly found to be proportional to the column density of interstellar hydrogen, N_H, since dust and cold gas seem to co-exist in many environments.

$$E(B-V) = \frac{N_H}{5.8 \times 10^{25} \text{ m}^{-2}}$$

In general

$$E(B-V) \sim 0.53 \text{ (d/kpc) and } A_V \sim 1.6 \text{ (d/kpc)}$$

for a line of sight of length, d, in kpc.

Optical emission from AGN can be dominated by emission from their nuclei (Figure 2.15). The discovery of Seyfert galaxies was notable due to their extremely bright optical nuclei that made them resemble bright stars. Many AGN have very strong optical emission lines originating in gas clouds. Diagnostic information derived from AGN emission lines provide information about the origin and excitation of such lines via starburst or non-thermal processes. For example, ratios of line strengths (i.e. [O I]/Hα vs. [O III]/Hβ) help discriminate the origins of emission lines between H II regions powered by UV radiation from hot, young stars and various shock-front, high energy excitation processes such as supernovae, jets or gas cloud-gas cloud collisions.

In many AGN both the emission lines and integrated stellar emission are swamped by much stronger synchrotron emission that increases its dominance on the total energy output as it progresses to longer wavelengths.

2.5.5   Infrared

Near-IR: 0.8-7 μm; Mid-IR: 7-25 μm; Far-IR: 25-300 μm.

Near-IR radiation can originate from stellar (i.e. cooler K and M type star) sources as well as being re-processed by dust. Mid-IR and Far-IR emission can be dominated by radiation from interstellar dust grains such as carbon, hydrocarbons, silicates, Polycyclic Aromatic Hydrocarbons (PAHs) heated by nearby stars. The IRAS wavebands in the Mid-IR (12 μm and 25 μm) detect radiation which is dominated by non-thermal emission from small grains. The exact origin of this emission is still uncertain, however it may be a mixture of warm ($\sim$50 K) dust associated with star forming regions, and cool ($\sim$20 K) dust associated with regions rich in atomic hydrogen, H I. The uncertainties are compounded by the unknown nature of the dust grain size and composition. Infrared 'cirrus' is faint, wispy cloud-like emission (first discovered in IRAS images) seen above and below the plane of the Galaxy. This is believed to be emission from dust clouds associated with nearby H I clouds.

Strong IR emission is detected in starburst galaxies, interacting or merging galaxies and AGN. IR observations are particularly important in terms of determining the source of emitted radiation. The IR emission can be used to probe dusty areas such as the inner regions of AGN, as well as regions of high star formation (e.g. in starbursts and mergers) that are not visible or heavily obscured in the optical.

Hydrogen recombination lines, especially Brα (4.05 μm) and Brγ (2.17 μm) of the Brackett series, and Pα (1.88 μm) of the Paschen series are frequently observed. Other Near-IR features include [Fe II] (1.64 μm), H_2 [15](J=1$\rightarrow$0) (2.12 μm), H_2 (J=2$\rightarrow$1) (2.25 μm) and CO (2.34 μm).

2.5.6 Submillimeter

300 μm -1mm.

Dust dominates the source of emission in the submillimeter region. Observations in this wavelength region have recently opened up due to innovations in instruments and detectors. Figure 2.16 shows an 850 μm image (Tilanus, van der Werf and Israel 2000) of the Whirlpool galaxy, Messier 51. Spiral arm structure is clearly seen indicating the position of dusty star forming regions.
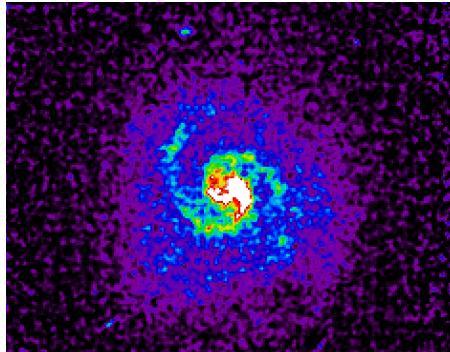

Figure 2.16: SCUBA image at 850 μm of the Whirlpool galaxy, NGC 5194 or Messier 51. NGC 5195 is seen to the north. Credit: JCMT/SCUBA. Image courtesy of R. Tilanus (JAC).

Submillimeter observations of distant starburst galaxies and AGN are very important. As discussed more fully in Section 2.7, emission detected at a particular wavelength from distant galaxies originates at shorter wavelengths at the source due to cosmological expansion. Hence submillimeter observations of distant galaxies can detect source emission in the IR. For example detection at 850 μm of a galaxy with a redshift $z = 2.4$ will sample emitted radiation at 250 μm, or from the Far-IR.

---

[15]Molecules move in space, at various speeds and directions. The energy and orientation of a molecule's tumbling motion is described as a rotational state, and these states are quantized. A molecule can spontaneously drop from its current energy state to the next lower one (i.e. a transition), converting the energy into a photon. The symbol (J=1$\rightarrow$0) and others like it denote the particular energy level transition.

2.5.7   Radio

1mm and longer wavelengths.

Radio recombination[16] lines of hydrogen such as H41α (92 GHz, 0.33cm), H29α (256.3 GHz, 0.11cm), H27α (316.4 GHz) and H26α (354.5 GHz) are important diagnostics of ionized gas conditions such as temperatures and electron densities. Figure 2.17 shows continuum emission at 92.0 GHz near the hydrogen recombination line of H41α in the starburst galaxy, NGC 3034/M 82.
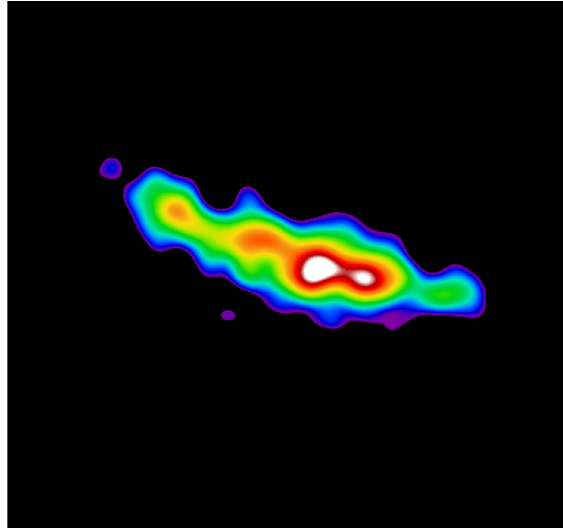

Figure 2.17: OVRO image at 92.0 GHz of NGC 3034/M 82. Credit: OVRO. Image courtesy of E. Seaquist.

The measurement of CO is believed to directly indicate the mass of Giant Molecular Clouds (GMCs) and can be used to estimate the amount of molecular hydrogen, H_2 (that is mostly cold, 10-20 K and hence not directly observable - the 2.12 μm line is from warm H_2). Whilst the 2.6 mm CO (J=1$\rightarrow$0) transition is most commonly observed, other lines such as 1.3 mm CO (J=2$\rightarrow$1) and 0.88 mm CO (J=3$\rightarrow$2) are studied as well. The Galactic factor, α, for the conversion between CO flux and H_2 column density[17]

$$\alpha = \frac{N_{H_2}}{S_{CO}} \text{ cm}^{-2} \text{ K}^{-1} \text{ km}^{-1}\text{s}$$

is given by (Omont 2007) as

$$\alpha = (1.8 \pm 0.3) \times 10^{20} \text{ cm}^{-2} \text{ (K km s}^{-1})^{-1}$$

---

[16]Radio recombination lines occur via transitions of electrons between two energy states with very high quantum number n. These lines are named after the atom, the destination quantum number and the difference in n of the transition (α for $\delta n = 1$, β for $\delta n = 2$, etc.). An example is H41α (transition from n = 42 to n = 41 in hydrogen).

[17]Column densities indicate the areal density of a given species, usually quoted in atoms cm^{-2}. N_n is the line integrated density of atoms in the nth state. Therefore N_{H_2} is the column density of molecular hydrogen.

for large molecular clouds away ($|b| > 5°$) from the Galactic plane and the molecular mass M_{mol} and CO flux S_{CO} are related by

$$M_{mol} = 1.61 \times 10^4 \, D_{Mpc}^2 \, S_{CO} \, M_\odot$$

Theoretical studies suggest that α could be a strong function of metallicity, density and excitation temperature.
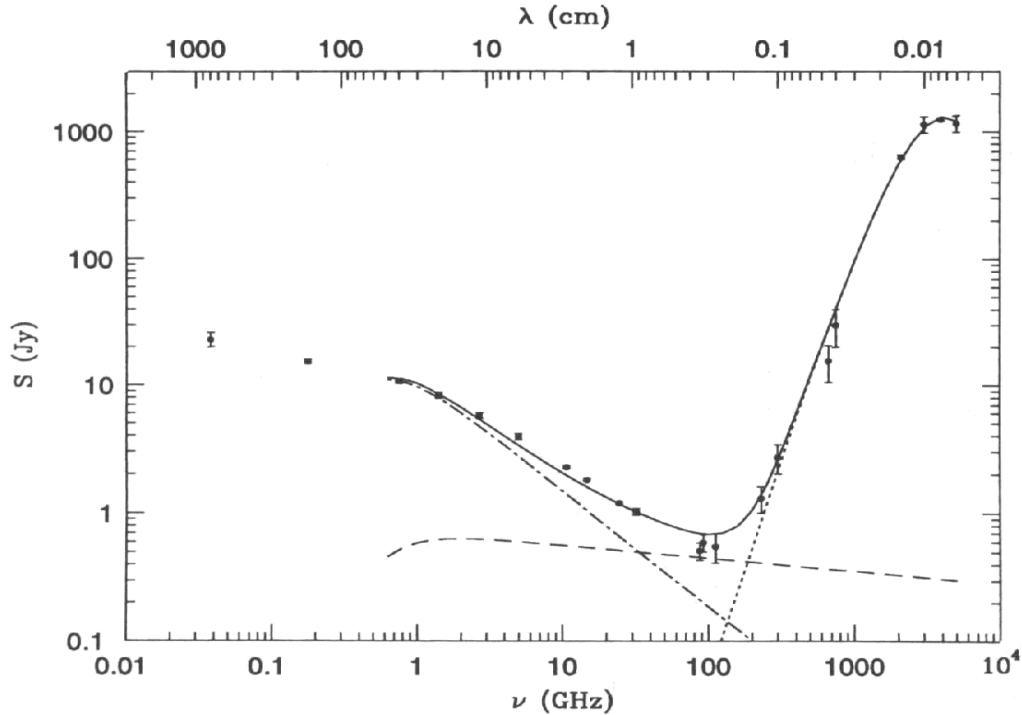

Figure 2.18: Radio/submillimeter/Far-IR spectrum of NGC 3034/M 82. The observations (data points) are fitted by a model (solid line) that consists of synchrotron (dot-dash line), free-free (dashed line) and dust (dotted line) components. Credit: With permission, from the Annual Review of Astronomy and Astrophysics, Volume 30 ©1992 by Annual Reviews www.annualreviews.org

Radio continuum emission can consist of non-thermal synchrotron radiation. Synchrotron radiation originates from old ($>10^7$ yr) relativistic electrons which have typically travelled significant distances from their parent SNRs. Powerful synchrotron emission can also be observed as core, jet or lobe emission due to nuclear activity in AGN (as described in Section 1.5.5). Some of the continuum radiation can also be thermal radiation from star formation or warm gas regions due to free-free[18] interactions of electrons. Carilli *et al.* (1991) investigate the energetics of the radio emission in Cygnus A and confirm the jet model for powerful radio galaxies. A

---

[18]When an electron collides with an atom or ion, and quantum mechanically emits or absorbs a photon.
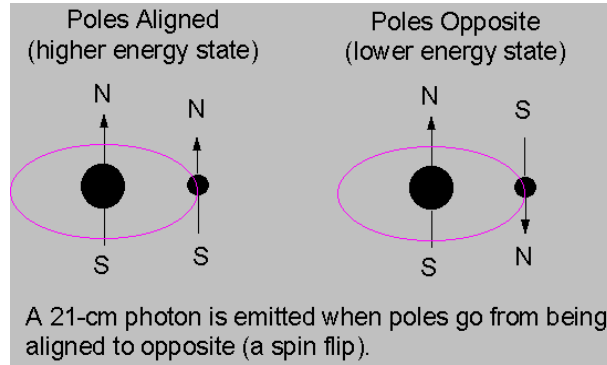
Figure 2.19: Emission of 21 cm radiation from the hydrogen atom. Credit: T. Herter.

synchrotron aging process occurs in which energetic particles are made at the radio hot spots, expand into the radio lobes and lose energy via the synchrotron process.

The complexity of emission in the starburst galaxy NGC 3034/M 82 is shown in the radio/submillimeter/Far-IR spectrum depicted in Figure 2.18. The radio region is at left, the Far-IR at right and the submillimeter region between wavelengths of 0.1 and 0.03 cm. The observed spectrum (data points) is well represented by the solid line model that is comprised of three different model emission mechanisms. This combined model is made up of synchrotron (dot-dash line), free-free (dashed line) and dust (dotted line) components. The synchrotron radiation dominates at wavelengths greater than 10 cm. The starburst induced free-free emission dominates between 30 and 200 GHz. Re-radiated emission from dust dominates the spectrum at frequencies greater than 200 GHz or wavelengths less than 1 mm in the submillimeter and Far-IR regions. The complete spectrum of NGC 3034/M 82 is shown in Figure 5.4.

Radiation from atomic hydrogen (H I) is emitted at the radio wavelength of 21[19] cm. This radiation occurs when the hydrogen atom changes from a high to low (preferred) energy state, as its electron changes its spin direction. Figure 2.19 depicts the relative spin directions of the proton and electron. This emission is called line radiation, because of its narrow wavelength distribution. The detection of H I shows the neutral (non-ionized) cold gas distribution (Figure 2.20) and identifies gas motions based on the detected wavelength of the 21 cm line. The H I mass of a galaxy can be calculated by

$$M_{HI} = 2.36 \text{ x } 10^5 \text{ D}^2_{Mpc} \text{ } \Sigma\Delta V \text{ M}_\odot$$

where D_{Mpc} is the distance to the galaxy in Mpc, $\Sigma\Delta V$ is the integrated line flux in Jy km s^{-1}, where Jy is Jansky, the unit of flux.

The H I mass of disk (spiral) galaxies normalized by their optical luminosity, M_{HI}/L_B, tends to increase in a systematic way from $\sim$0.05 $M_\odot/L_\odot$ for Sa spirals, to $\sim$1 $M_\odot/L_\odot$ for Magellanic irregulars (Sm and Im classes). Strong H I in ellipticals is

---

[19]Astronomers refer to this emission line as 21 cm - more accurately its vacuum wavelength is 21.11 cm and frequency is 1420.41 MHz.
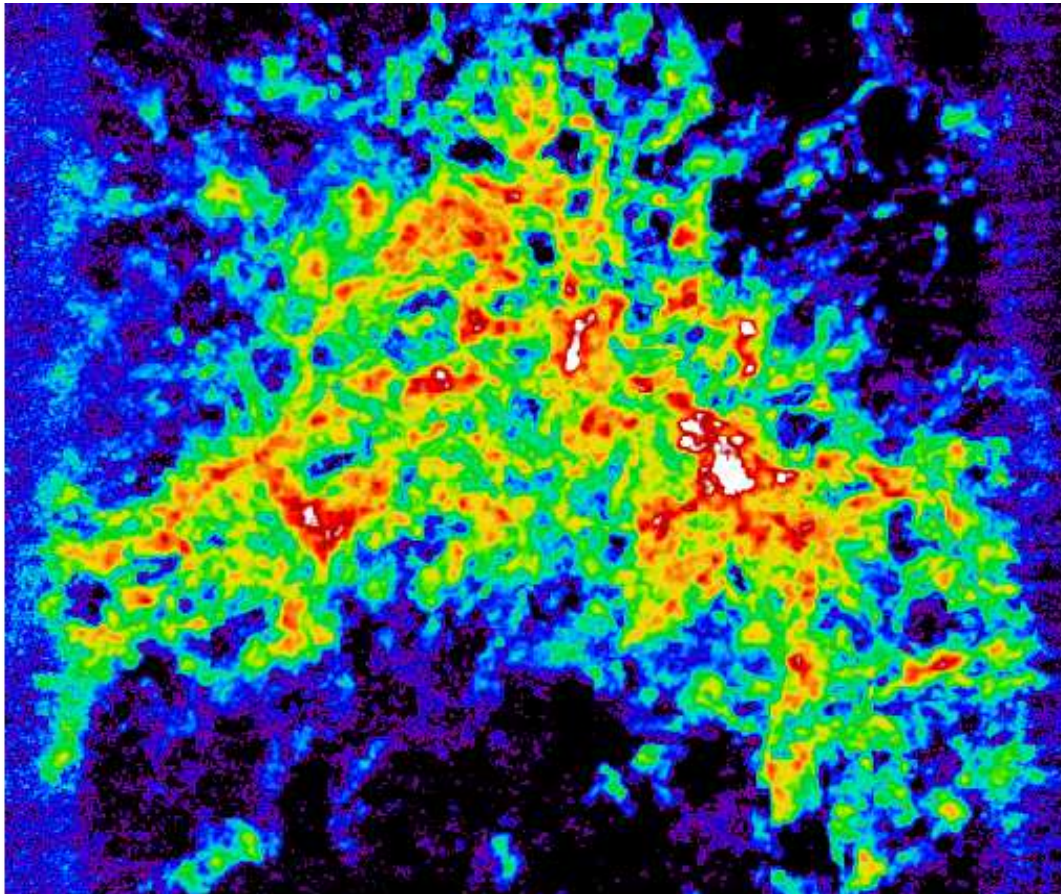
Figure 2.20: H I radio image of the Small Magellanic Cloud. This emission shows the distribution of cold, atomic hydrogen gas. R.A. spans 0h 25m (right, bottom) to 1h 40m (left, bottom). Dec. spans -70° 20′ (top) to -75° 10′ (bottom). The H I map was observed with ATCA, over 8 x 12 hours observing periods and has a spatial resolution of 98″. Credit: S. Stanimirovic, L. Staveley-Smith and CSIRO.

not common, though H I detections suggest that such cold gas may originate from gas rich galaxies that have merged with the elliptical.

2.6   Caveat #1: Mass versus Light and Dark Matter

> *I think many people initially wished that you didn't need dark matter. It was not a concept that people embraced enthusiastically. But I think that the observations were undeniable enough so that most people just unenthusiastically adopted it.*

> *Vera Rubin*

This atlas shows images which depict various types of radiation originating in or near galaxies. However, when considering the total amount of matter in these objects, observations only directly detect radiation from a small fraction of the total mass of each galaxy. Measurements of the velocities of gas (e.g. neutral hydrogen) as a function of radius in spirals, and the detection of hot, 10^7 K, gas around ellipticals, imply that dynamically inferred galaxy masses are a factor of ∼5 or greater than the masses deduced from the combined luminosities of the stars and gas. In fact the atlas galaxy NGC 2915 (page 146) has a dark matter content probably a factor of 50 greater than its luminous matter, suggesting that dark matter makes up ∼98% of the total galaxy mass.

In a sense observations only detect the tip of each galactic 'iceberg', with the majority of the mass of each galaxy remaining unseen. The first quantitative study of this unseen matter was carried out early in the 20th century (Oort 1932) by observing the vertical motions of stars in our Galaxy. The local mass density near the Sun was initially determined to be ∼0.15 $M_\odot$ pc^{-3}, with dark matter representing 40% of the total local mass, although by the 1980s this was shown to be an overestimate.

Early observations of the Andromeda galaxy also showed discrepancies between dynamical and luminosity based masses. The rotation curve of NGC 224/M 31 (Babcock 1939) implied a *global* mass-to-light ratio (M/L) of ∼14 (corrected for the present day distance to NGC 224/M 31), which was a factor of 10 higher than that implied at the nucleus. The discrepancies were even larger in the case of galaxy clusters. Observations of clusters showed individual galaxies with much larger radial velocities than could be accounted for assuming a gravitationally bound cluster. Smith (Virgo cluster; Smith 1936) and Zwicky (Coma cluster; Zwicky 1937) detected a large mass discrepancy in these nearby clusters. In a landmark study of disk galaxies (Freeman 1970) Ken Freeman commented on the rotation curves of M 33 and NGC 300 and noted that they did not show an expected Keplerian velocity decline[20] their optical radii:

---

[20]If the total mass converges at some radii, the rotation curve would behave as V $\propto \frac{1}{r}$, in which velocities at large r would eventually decline.

> *For NGC 300 and M 33 ... there must be in these galaxies additional matter which is undetected, ... Its mass must be at least as large as the mass of the detected galaxy, and its distribution must be quite different from the exponential distribution which holds for the optical galaxy.*

> *Ken Freeman*

Freeman had re-kindled the question of dark matter, this time though *in galaxies*, and was also the first to speculate on its structure. In the mid-1970s Rubin and colleagues observed rotation curves of spirals that were flat or even rising to large radii that finally brought the problem to wide attention.

Theoretical models suggest large, massive dark matter halos exist around most if not all galaxies. The size of the halos may be very large. For example, whilst the distance between the Galaxy and NGC 224/M 31 is $\sim$700 kpc and if the luminous diameters of both galaxies are $\sim$40-50 kpc, (but see below) a large fraction of the intervening distance could be taken up with their individual dark matter halos. The dark halos may even overlap.

Deep exposure imaging (McConnachie *et al.* 2009), Figure 2.21, around NGC 224/M 31 and towards its Local Group neighbor NGC 598/M 33 has shown stellar structure extending 150 kpc from NGC 224/M 31 and overlapping with stellar light extending 50 kpc from NGC 598/M 33. It is likely that stars exist between both galaxies and could exist as far away from parent galaxies as the virial radius of their dark matter halos ($\sim$300 kpc for NGC 224/M 31).

The virial theorem relates the total kinetic energy of a self-gravitating body due to the motions of its constituent parts, K to the gravitational potential energy, U of the body such that 2K + U = 0. For gravitationally bound galaxies in equilibrium, and with some assumptions the relationship

$$M = \frac{2v^2R}{G}$$

follows, where M is the total mass of the galaxy, v is the mean velocity (the sum of the rotation and velocity dispersion) of stars in the galaxy, G is Newton's gravitational constant and R is the effective radius (size) of the galaxy. Defining the virial radius is somewhat more complicated. For an equal mass system, the virial radius r_v is the inverse of the average inverse distance between particles, r, in an N-body system. For a general system of i particles with masses, m and total mass M, the definition is

$$\frac{M^2}{r_v} = \sum_i \sum_{j,j\neq i} \frac{m_i m_j}{|r_i - r_j|}$$

For simplicity r_v can be thought of as the radius of a sphere, centered on a galaxy or a galaxy cluster, within which virial equilibrium holds. In practical terms it is often approximated as the radius within which the average density is greater, by a
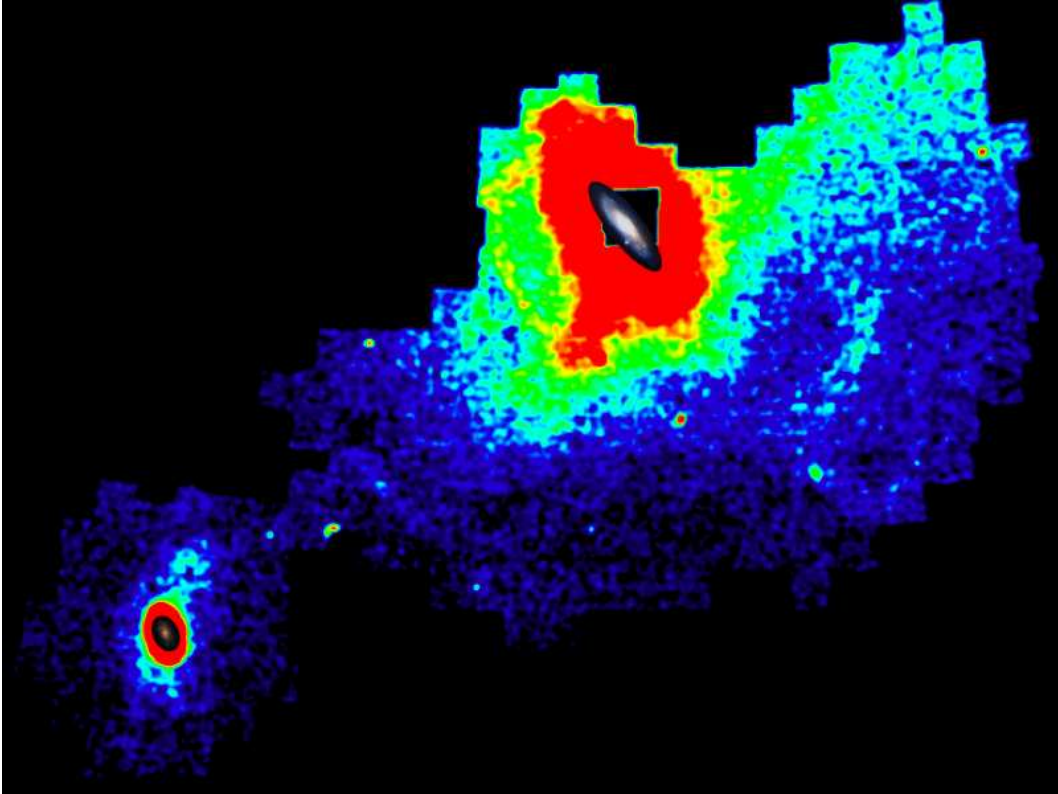
Figure 2.21: Stellar density map of the Andromeda-Triangulum region. A projection of the stellar density distribution with scale images of the disks of NGC 224/M 31 (top, right) and NGC 598/M 33 (bottom, left) overlaid. Credit: A. McConnachie. The small images of M 31 and M 33 courtesy T. A. Rector, B. A. Wolpa and M. Hanna (NRAO/AUI/NSF and NOAO/AURA/NSF). Reprinted by permission from Macmillan Publishers Ltd: Nature, vol. 461, p. 66., copyright (2009).

specified factor, than the critical[21] density

$$\rho_{\mathrm{crit}} = \frac{3\mathrm{H}_0^2}{8\pi\mathrm{G}}$$

where H_0[22] is the Hubble constant. A common choice for the (over) density factor to describe r_v is 200 (early simulations suggested that the radius at a density factor of 178 is close to r_v) in which case r_v is approximated as r_{200}.

The extended stellar distributions comprise both individual stars lost from each system during previous nearby interactions and the destroyed remnants of dwarf galaxies due to the tidal field of each galaxy. These observational signatures are

---

[21]The mass density below which the universe is open (positive space curvature), and above which the universe is closed (negative space density) is the critical density. It is approximately $\rho_{\mathrm{crit}} = 1.0 \times 10^{-26}$ kg m^{-3}.

[22]The linear relationship between a galaxy redshift and its distance, is commonly specified as $\mathrm{H}_0 = 100h$ km s^{-1} Mpc^{-1}, the Hubble constant. The dimensionless quantity h, until recently was taken to be between 0.5 and 1.0, but now appears to be close to 0.72.

consistent with galaxy growth inside dark matter halos that grow via accretion and mergers events.

Candidates for the origin of dark matter, both of baryonic[23] (e.g. black holes, brown dwarfs and white dwarfs) and non-baryonic (e.g. neutrinos with mass) forms, are numerous. Current models of dark matter and computer simulations of large-scale structure compared to observed structure suggest that the majority of dark matter is 'cold'. Cold Dark Matter (CDM) would comprise slow moving, massive particles. In comparison Hot Dark Matter (HDM) would consist of fast moving, light particles. Experiments suggest that neutrinos could have mass and could therefore be a candidate for HDM, but are probably not massive enough to be a dominant part of dark matter. Primack (2009) presents an overview of dark matter in relation to galaxy formation in the context of the ΛCDM 'Double Dark' standard cosmological model. 'Darkness' appears to rule the universe. CDM plus 'dark energy' (denoted by Λ; the unknown force or property of the vacuum driving the acceleration of the universe) make up 95% of the cosmic density. The search for the origin of dark matter continues.

2.7 Caveat #2: Looking Back to the Beginning

Detecting galaxies at cosmologically large distances introduces several observational biases.

Firstly, because of the expansion of the universe and the Doppler effect their emitted radiation is detected at longer, redshifted[24] wavelengths. For example, the optical Hα emission line (emitted at $\lambda = 6563$Å, in the rest-frame) in a galaxy at redshift z = 1 will be detected by a telescope at $\lambda = (1 + z) \times 6563$Å $= 13,126$Å (1.3126 μm in the Near-IR).

Sources observed at different redshifts are sampled at different rest-frame wavelengths. Photometry is performed with a fixed bandpass filter, so the effective width of the bandpass will change with different source redshifts. The correction for this effect, which transforms a measurement of a source at a redshift z, into a standard measurement at redshift zero or the rest-frame, is called the 'K correction'. It is dependent on galaxy type and redshift.

For a source observed with an apparent magnitude m_Y, through the photometric bandpass Y, which has an absolute magnitude M_C in an emitted frame bandpass C, the K correction $K_{CY}(z)$ is defined by

$$m_Y = M_C + DM + K_{CY}(z)$$

where DM is the distance modulus of the source, defined as

$$DM = 5 \log_{10} \frac{D}{10 \text{ pc}}$$

---

[23] A massive elementary particle made up of three quarks. Neutrons and protons are baryons.

[24] The vast majority of galaxies are redshifted. A few, nearby galaxies such as NGC 224/M 31, that are influenced by local gravitational fields, are approaching us, and their radiation is blueshifted to smaller wavelengths.

and D is the source distance in pc. For galaxies that can be described by a power law

$$F_\nu \propto \nu^{-\alpha}$$

where α is the power-law index and F is the specific flux then

$$K_{CY}(z) = 2.5\,(\alpha - 1)\,\log_{10}(1 + z)$$

Secondly, at very large distances the inverse-square law of radiation propagation fails as the radiation surface area is no longer described by a wavefront on a normal sphere surface. A consequence of this is that the surface brightness of an extended, distant object is redshift dependent and scales as $(1+z)^{-4}$. This is known as cosmological or Tolman dimming. The large exponent ensures this effect is quite drastic even at $z \sim 2$ when the cosmological dimming factor of surface brightness is 81.
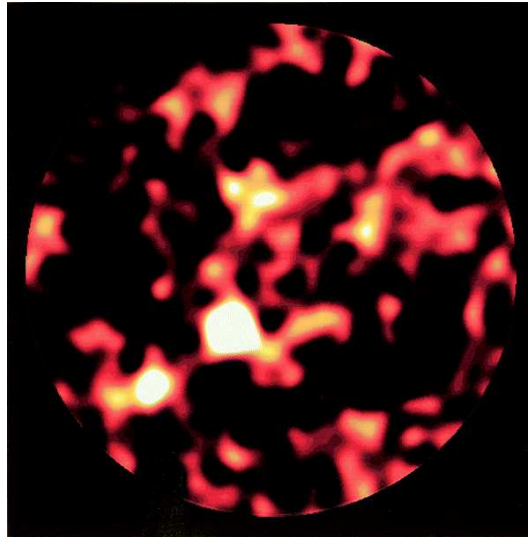

Figure 2.22: JCMT SCUBA 850 μm image of the Hubble Deep Field - North. The radius of the field is $100\,''$. The field is centered at 12h 36m 51.2s, $+62°\ 12'\ 52.5\,''$ J2000. Five sources have been identified with galaxies. Data from Hughes *et al.* (1998). Credit: Reprinted by permission from Macmillan Publishers Ltd: Nature, vol. 394, p. 241., copyright (1998).

Thirdly, there is an age or evolutionary effect. Due to the substantial light travel times to distant galaxies their radiation is detected when they were at much younger ages. Stellar populations evolve, thus as more and more distant galaxies are detected, the radiation from successively younger and younger populations are recorded.

A long exposure image by HST WFPC2 in the constellation of Ursa Major is known as Hubble Deep Field-North (HDF-N). Four filters (F300W, F450W, F606W, and F814W), spanning the Mid-UV through optical to Near-IR region were combined to give a 'true-color' view of the distant universe. A sight line out of our Galaxy with a low density of foreground Galactic stars supplied a clear view. The

majority of objects in the image are distant galaxies, some with z ~ 3, implying light travel times of ~10 Gyr. Ignoring stellar population evolution, for galaxies at $z = 3$, observed in the F814W filter ($\lambda = 8140$Å) observations detect emitted (at the galaxy) radiation of $\lambda = (8140$Å$/1 + z) = 2035$Å, which is in the Mid-UV. Such effects have to be taken into account when observing distant objects.

Figure 2.23: Hubble Ultra Deep Field - Infrared. A 48 hour integration by HST WFC3 in the constellation of Fornax. Three filters (F105W - blue, F125W - green and F160W - red) are combined. The majority of objects are distant galaxies. The image is ~2.4′ across. Credit: NASA, ESA, G. Illingworth (UCO/Lick Observatory and UCSC), R. Bouwens (UCO/Lick Observatory and Leiden Univ.) and the HUDF09 Team.

Since detected radiation is redshifted by significant amounts from distant galaxies it is worth observing these galaxies at IR and longer wavelengths. Many galaxies are strong emitters in the optical and Near-IR regions which will help in the detection of distant sources. Such wavelength regions will also contain re-emitted radiation from dusty sources. Since many distant, young galaxies and starburst galaxies will have high dust contents due to intense star formation, the submillimeter is an excellent region to utilize. Figure 2.22 is a JCMT SCUBA image of the HDF-N at 850 μm.

After fifty hours of integration time this image represents one of the deepest submillimeter images ever taken. Five discrete sources have been identified with galaxies, four of which are likely to be galaxies with redshifts in the range $2 < z < 4$. The submillimeter results indicate that the star formation rates in these distant galaxies are about five times higher than that indicated by the UV properties of the HDF-N galaxies. This result highlights the importance of the submillimeter region as an accurate indicator of star formation for distant galaxies.
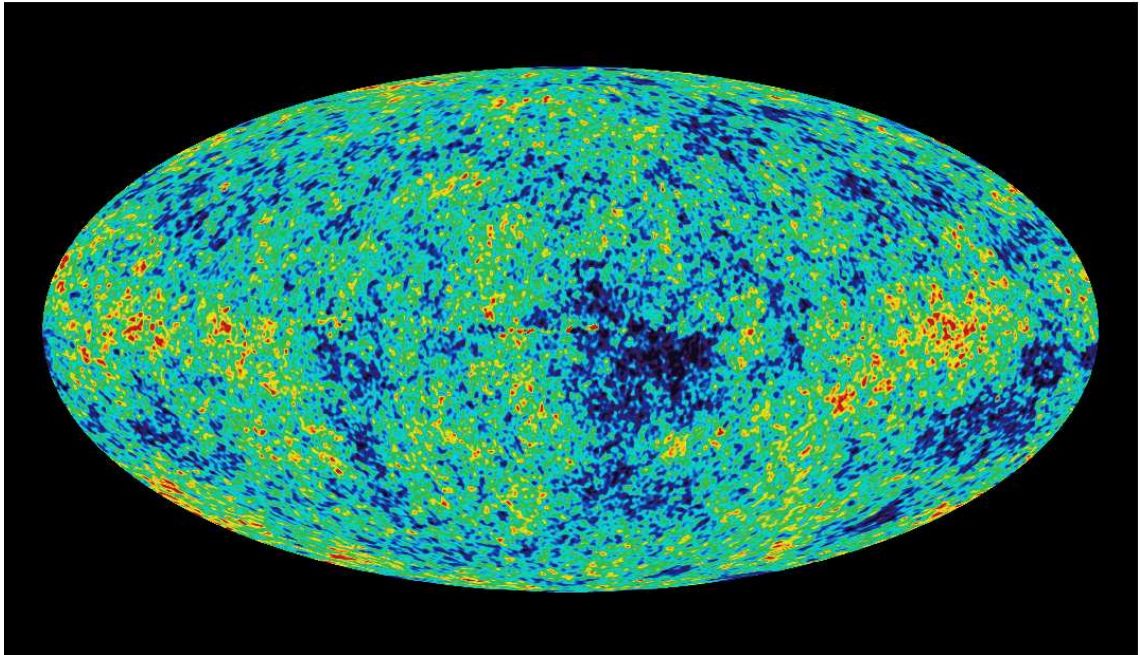
Figure 2.24: The all-sky Cosmic Microwave Background observed by WMAP. Credit: NASA/WMAP Science Team.

Not to be outdone, CXO has also observed this region of sky. About 556 hours (twenty-three days!) of observations were combined in the Chandra Deep Field North image. Many of the objects detected are AGN with SMBHs. This data is being used to determine when such black holes form and how they evolve. The data shows that SMBHs are quite rare at the very earliest times in the universe suggesting that they need time to grow by feeding on gas and stars. Detecting X-ray photons is difficult! The faintest sources in the image produced only *one* X-ray photon every four days.

The power of observing distant galaxies at longer wavelengths is dramatically shown in Figure 2.23 which is a long exposure of the Hubble Ultra Deep Field using HST WFC3 Near-IR filters with wavelength centers of 1.05, 1.25 and 1.55 μm. Comparison should be made with Figure 1.18 which was a predominantly optical image of the same area of sky. The WFC3 Near-IR image shows numerous small, red objects - not seen in the ACS optical-based image - many of these are distant galaxies, seen ∼600 million to 1 Gyr after the Big Bang.

Figure 2.24 is an image of galaxies and clusters of galaxies in the making. It shows the sky in the microwave region, expressed as minute fluctuations in temperature above and below (red and blue respectively) the Cosmic Microwave Background (CMB) temperature of 2.73 K.

The CMB all-sky emission at 2.73 K was detected and understood in 1965 as remnant radiation from the Big Bang start to the universe. The Big Bang 'fireball' has expanded and cooled after 14 Gyr and this remnant radiation has the temperature and blackbody characteristics consistent with such a hot beginning. What exactly is

seen in Figure 2.24? Our early universe consisted of a dense, hot 'soup' of sub-atomic particles and extremely high-energy photons interacting with one another. As the fireball expanded the density and temperature decreased. Small, weak density variations evolved, and altered the temperature of the photons. Lower density regions are the temperature hot spots in the CMB and higher density regions correspond to colder regions.

About 300,000 years after the Big Bang, the temperature had reduced to 3,000 K which was cold enough so that sub-atomic particles (i.e. protons, neutrons, electrons) could combine to form atoms. Photons could then travel without significant scattering or absorption and the universe became 'transparent'. The last interactions of photons with matter, in particular electrons, occurred at this time (300,000 years corresponds to a redshift of $z \sim 1000$) and this is what is observed as the CMB. It is called the last scattering surface and it is the signature of the universe at the time the first structures of matter formed. Gravity then took over and galaxies eventually formed. Hence the CMB is an important link between the hot, smooth early universe devoid of galaxies and the much cooler, lumpy universe full of galaxies today.

In the early 1990s the Cosmic Background Explorer (COBE) satellite discovered small (ten parts in a million) differences in the CMB temperature across the whole sky. These deviations are very important since they are needed if structures such as clusters of galaxies and individual galaxies are to form. However the angular resolution of $\sim 7°$, for COBE was not sufficient to determine the smallest sizes of these deviations. In late 1998 the Balloon Observations of Millimetric Extragalactic Radiation and Geophysics experiment or BOOMERANG, was launched in the Antarctic and circumnavigated the continent at an altitude of ~ 37 km for about 10 days. BOOMERANG delivered observations with an angular resolution of $\sim 0.2°$ and sampled over 3% of the sky.

The Wilkinson Microwave Anisotropy Probe (WMAP) was launched on June 30th, 2001 and has produced all-sky microwave maps (Figure 2.24) with BOOMERANG-like angular resolution ($\sim 0.3°$) providing the best yet information about early universe structure formation and evolution. It has provided an estimate of the age of the universe of 13.69±0.13 Gyr as well as baryon, dark matter and dark energy density, Hubble constant, H_0 and total neutrino mass (Dunkley *et al.* 2009).

2.8 Caveat #3: Observational Bias

All scientific measurements have an inherent bias. The selection of a particular telescope, instrument and detector combination will bias astronomical detections, whether it be due to the diameter of the telescope mirror, the wavelength of detection, the length of the observation, or the efficiency and characteristics of the detector.

A clear-cut example of sample bias is found in most surveys of distant galaxies. Galaxies close to the detection limit (i.e. at the faint limit of the survey) will be more luminous on average than those at a brighter limit. Simply put, towards fainter

levels of detection, which usually means detecting more distant galaxies, it becomes progressively more difficult to detect intrinsically faint objects, and the sample gets skewed towards more luminous objects. This is known as 'Malmquist bias' and it affects all galaxy surveys that are flux limited.

Galaxies are diffuse, extended objects. They are detected against the competing brightness of the night sky, which is typically 23 magnitudes per square arcsecond (mag arcsec^{-2}) in the optical B. Depending on your observational set-up, below a certain fraction of the night sky brightness no galaxy will be detected. A 'censorship of surface brightness' exists and until recently most studies of galaxies would tend to concentrate on the brighter surface brightness examples. There is however increasing efforts to detect and study Low Surface Brightness (LSB) galaxies. Although there is no formal convention for defining an LSB galaxy, they typically have central surface brightness fainter than 23 B mag arcsec^{-2}.

Malin 2 (page 149) is an example of a LSB galaxy. LSBs are made up of a variety of galaxy types, from giant, gas-rich disk galaxies (i.e. Malin 2) to dwarf spheroidal galaxies. The extreme ultra gas rich LSB galaxies have similar properties to small groups or clusters of galaxies, suggesting they have experienced a different evolution history than their high surface brightness cousins.

2.9 Galaxy Research and Multiwavelength Observations

There are numerous areas in galaxy research that owe their existence to the power of panchromatic observations. Many of these areas are still being pursued as open areas of research and the following sections describe a few of these areas.

2.9.1 A Unified Scheme of Active Galaxies

Attempts have been made to show that the numerous AGN classifications and properties can be explained by a 'Unified Scheme'. This scheme (Antonucci 1993; Urry and Padovani 1995) suggests that the differences seen in AGN can be accounted for by observing the same type of active galaxy along different lines of sight through different orientations of a similar central structure.

In the Unified Scheme (Figure 2.25) every AGN contains an obscuring dust and gaseous doughnut-like torus around a central supermassive black hole (SMBH) that has a surrounding thin gaseous accretion disk. Highly collimated relativistic jets are produced at right angles to the plane of the dusty torus. Observing the nucleus via a line of sight that intersects the plane of the torus would obscure the active core of the accretion disk and SMBH. It would appear as a Radio Galaxy, for an elliptical host galaxy, or as a Sy 2, for a spiral host galaxy.

Up to a distance of several kpc from the nucleus are the gaseous 'narrow line regions' (NLR) excited either by photoionization from the UV continuum of the central source or by shock excitation related to the jets. The gas clouds visible would be predominantly far away from the nucleus, with low-density, slowly moving, having
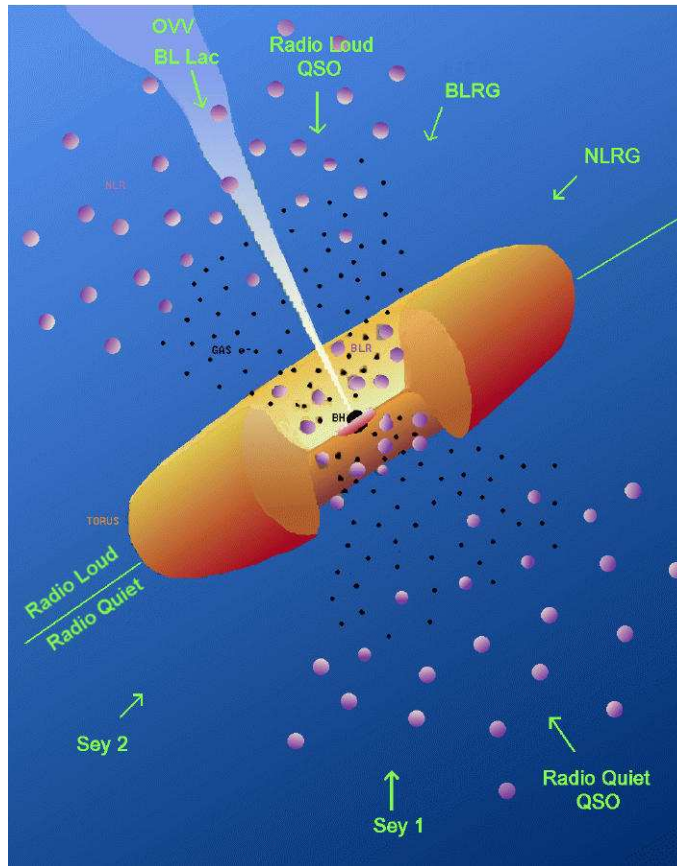
Figure 2.25: A schematic representation of the Unified Model of Active Galaxies. Various sight lines into the AGN are indicated. BLRG stands for Broad Line Region Galaxy; NLRG stands for Narrow Line Region Galaxy.

small line widths ($\sim$500 km s^{-1}). Alternatively, observing along the direction of the relativistic jet allows a clear view of the nucleus, so it would appear as a Blazar, or a Sy 1 for a spiral host. Gas orbiting close to the SMBH is photoionized, producing the Doppler-broadened emission lines characteristic of the 'broad line region' (BLR). The gas clouds are dense with typical speeds of 5000 km s^{-1}, thus having wide or broad line widths. Intermediate viewing angles could show an AGN with properties of a broad lined Sy 1, quasar or Radio Galaxy.

Shortfalls in the Unified Scheme can be explained by variations in the properties of the structural components. For example variations in black hole mass, the size and mass of the dust torus, galaxy gas content (i.e. possible fuel for a black hole), and the dynamical state of the host galaxy (Dopita 1997) could easily exist. Ho (2008) also promotes the idea that LINERs and other low luminosity AGNs may not be simple scaled-down versions of their higher luminosity relatives. Their central engines may be qualitatively different. Whilst the Unified Scheme does not explain all observed AGN characteristics it is the best model at present.

Supporting indirect evidence in favor of the Unified Scheme comes from observations of the cores of nearby elliptical galaxies. Large velocity gas motions close to

the nuclei in many galaxies indicate masses of $\sim 10^9$ $M_\odot$ inside an area not much larger than our Solar System that could be explained by the presence of a SMBH.
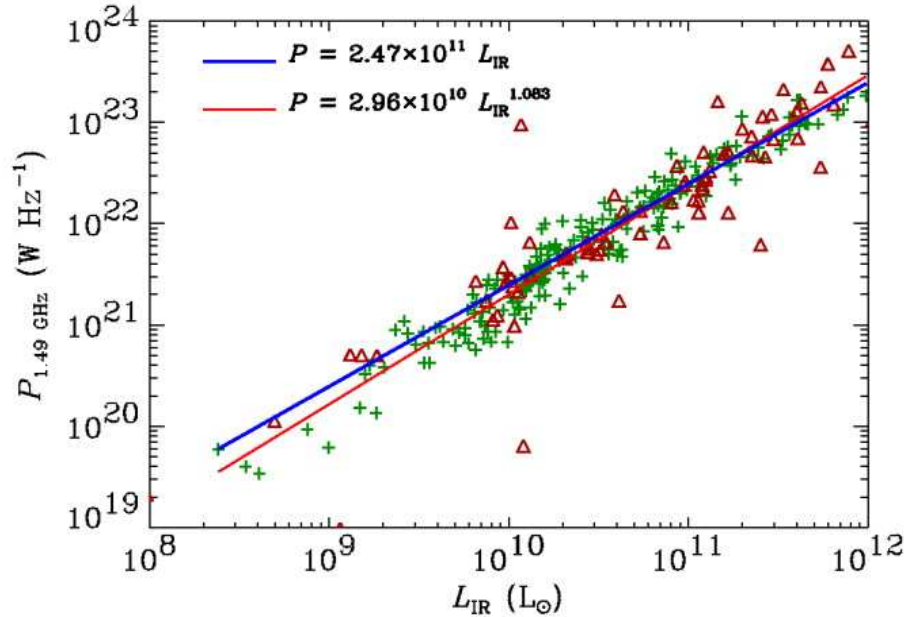
2.9.2   The Far-IR Radio Correlation

Figure 2.26: 1.49 GHz radio power versus Far-IR luminosity for IRAS galaxies. Credit: Data kindly provided by E. Dwek - original form in Dwek and Barker (2002). Reproduced by permission of the AAS.

A correlation was found between the Far-IR and radio continuum strengths of normal spiral galaxies (van der Kruit 1973). This initial finding was confirmed by the IRAS satellite. Using IRAS 60 and 100 μm flux densities the Far-IR flux of normal star forming galaxies is strongly correlated with their 20 cm radio flux. The Far-IR-radio correlation (Figure 2.26) ranges over five orders of galaxy luminosity. What is remarkable is that this very strong and universal correlation seems to originate from the same stellar population, high mass stars, giving rise to two very different emission mechanisms, one thermal, the other non-thermal. It is now established that the Far-IR emission is thermal and originates in dusty H II regions heated by high mass stars. The 20 cm luminosity is mainly synchrotron radiation from relativistic electrons accelerated in SNRs. This non-thermal radiation dominates any radio free-free (thermal) emission that may occur in ionized gas regions. For example, Figure 2.18 shows the dominance of synchrotron over free-free emission at 20 cm in NGC 3034/M 82. The SNRs are of course direct evolutionary consequences of the same high mass stars (Condon 1992).

Dopita (2005) discusses the correlation for starburst galaxies and summarizes that if the synchrotron electrons are short-lived compared to the starburst phase timescale, the synchrotron emissivity relates directly to the supernova rate which in

turn should be proportional to the SFR.

The linearity of the Far-IR radio correlation has been questioned. Bell (2003) has compared the Far-UV derived star formation rates with that from the Far-IR and found that the Far-IR traces most of the star formation in luminous $\sim L^*$ galaxies but traces only a small fraction of the star formation in faint $\sim 0.01 L^*$ galaxies. Since the Far-IR Radio correlation is very close to linear at low luminosities Bell (2003) suggests that the non-thermal radio flux is also decreased - which conspires to give such a linear correlation. This work is difficult for a number of reasons. Firstly, small numbers of low luminosity galaxies (usually selected or enhanced across non-homogeneous samples) are used in many such studies. Secondly, there are potential problems in relating UV-derived to other star formation rate indicators because of the different stellar timescales probed by the UV relative to other tracers of ionizing photons. Calzetti *et al.* (2007) study star formation based on Mid-IR emission of local galaxies and show that their viability as SFR indicators is subject to a number of caveats. The most robust star formation indicator combines the observed Hα and 24 μm luminosities as probes of the total number of ionizing photons present in a region.

2.9.3 A Non-Universal IMF

The initial mass function (IMF), $\xi(M)$, describes the mass distribution of stars formed in a particular region. It takes the form of a power law

$$\xi(M) = c\, M^{-(1+x)}$$

with $\xi(M)$ existing over a range of stellar masses - these limits have been $M_{lower} = 0.1\ M_\odot$ to $M_{upper} = 125.0\ M_\odot$ in three of the most popular IMFs (Salpeter 1955 with a slope of $x = 1.35$; Miller and Scalo 1979; Scalo 1986). Until recently it was assumed, possibly for simplicity, and somewhat naively, that the IMF was universal.

The results of Meurer *et al.* (2009) now challenge this assumption. Using a large sample of H I selected galaxies, the ratio of Hα to Far-UV flux is found to correlate with the surface brightness in Hα and the optical R. It is found that Low Surface Brightness (LSB) galaxies have lower Hα to Far-UV flux ratios than high surface brightness galaxies, and do not replicate the ratios derived from popular star formation models using IMF parameters (as above). The authors suggest the correlations are systematic variations of the upper stellar mass limit and/or slope (x) of the IMF at the high mass end. Simply stated, low luminosity galaxies have less massive stars than higher luminosity galaxies. Yet it appears that the surface brightness drives IMF variations more than luminosity or mass. These results imply that the rate of star formation derived is highly sensitive to the indicator used in the measurement, as mentioned in the previous section.

2.9.4 Gamma Ray Bursts

A GRB detected on May 8th, 1997 (GRB970508) by the BeppoSAX satellite was the first GRB for which a secure distance could be estimated. An associated optical

transient was detected 5.8 hours after the discovery (Djorgovski *et al.* 1997) and its brightness decline was consistent with relativistic 'fireball' models of extreme energy events. Spectroscopy of the optical transient (Metzger *et al.* 1997) showed absorption lines due to a galaxy at a redshift of $z = 0.84$. The absence of Lyman-α (hydrogen) absorption in the spectrum implied that the optical transient had a redshift between $0.84 < z < 2.3$. At the minimum redshift of $z = 0.84$, this GRB would have a total luminosity of 7×10^{51} erg s^{-1}. To put this in perspective, the luminosity of the *brief* GRB970508 event was equivalent to the optical luminosity of more than 10^8 galaxies similar to the Galaxy. A more recent burst, GRB090423, detected by the Swift satellite, is associated with a galaxy at z = 8.2. This implies that the GRB is being detected only after $\sim$5% of the age of the universe has expired.

Theoretical models have been proposed to explain the energy source and emission mechanism of these bursts. Candidate models include neutron star-neutron star or black hole-black hole mergers (or a combination of the two objects) and hypernovae that are extremely massive stars undergoing supernovae collapse to a black hole. These models usually rely on some sort of preferential beaming of radiation along our line-of-sight to achieve the observed extreme luminosities.

Observations have been strengthening the case for a GRB-Supernovae link. CXO detected a spectrum of hot gas moving at 0.1c for GRB020813 containing numerous elements commonly seen in the ejecta of a supernova explosions. The data appears to support the hypernovae model in which shock waves in jets emanating from the black hole region produce Gamma rays and X-rays. The CXO observations detect the radiation from the jets interacting with the expanding shells of ejected gas.

2.9.5   Magnetic Fields in Galaxies

Large-scale magnetic fields exist in spiral (grand design and flocculent[25]), irregular and dwarf irregular galaxies and are coherent over scales as large as 1 kpc. Their origin and evolution is directly linked to induction effects in the ionized ISM. These fields are likely driven by a large-scale dynamo action that can exist even whilst other hydromagnetic effects occur either globally (i.e. spiral arm related density wave propagation; bars), or locally (i.e. galactic fountains, shocks) (Beck *et al.* 1996; Krause 2003).

Continuum radio observations allow the detection of galactic magnetic fields via synchrotron emission. The intensity of linearly polarized emission measures the magnetic field (Figure 2.27), after correction for Faraday rotation and depolarization[26]. Observations at two or more frequencies allows the correction to be computed.

Regular magnetic fields align with spiral arms but are strongest in the inter-arm regions. Total field strengths are on average 8 μG[27] with some inter-arm regions

---

[25]Flocculent spirals have patchy disk structures rather than clear spiral arms.

[26]The rotation of the plane of polarization of a linearly polarized wave propagating through a magnetized dielectric medium is known as Faraday rotation (discovered by Michael Faraday in 1845). The rate at which the plane of polarization rotates is proportional to the product of the electron number density and the parallel magnetic field strength.

[27]G stands for gauss, the cgs unit of measurement of a magnetic field, named after Carl Friedrich
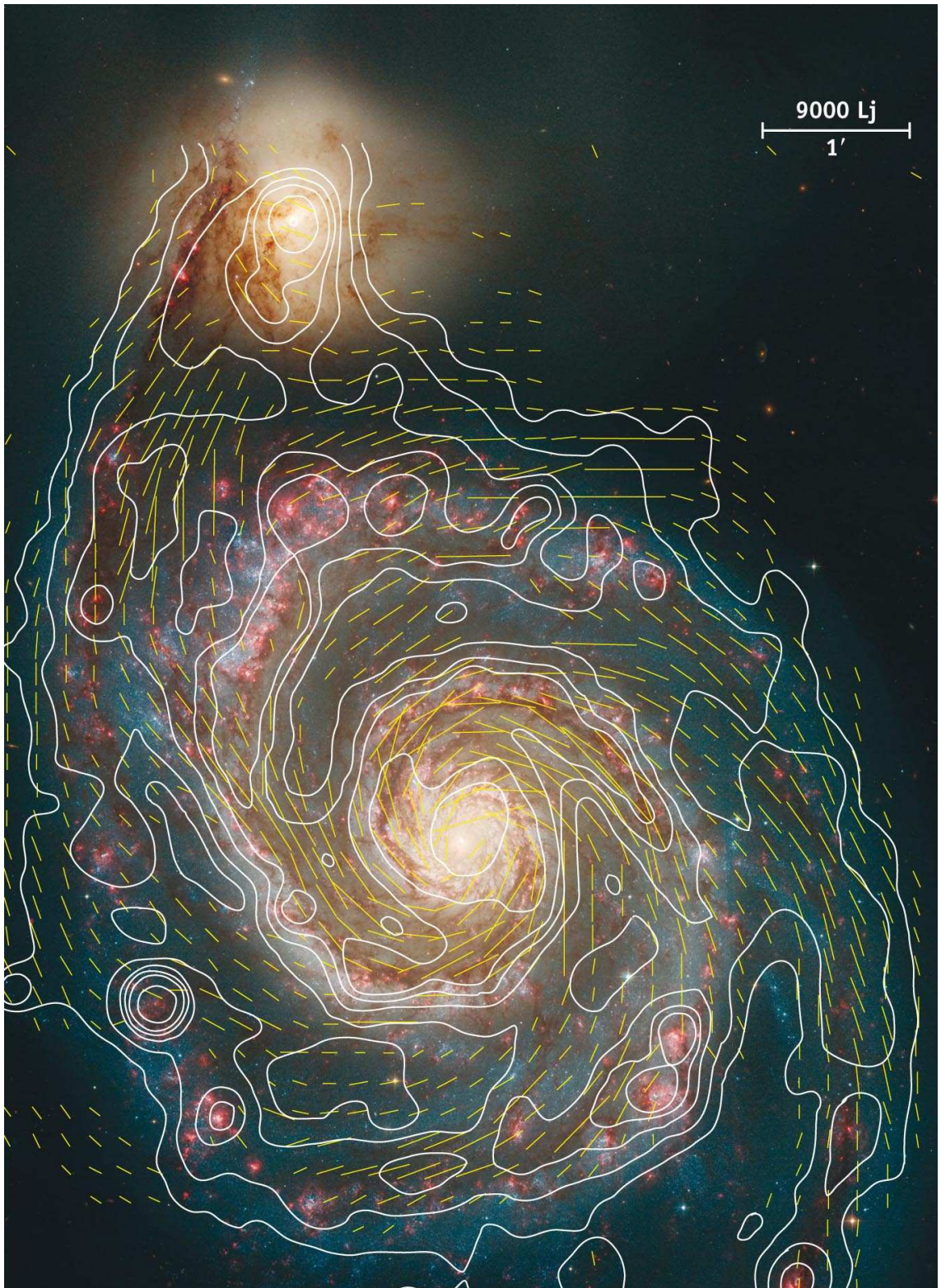
Figure 2.27: The magnetic field of NGC 5194/M 51 overlaid on the optical. Credit: Radio continuum (white contours) and magnetic field (yellow vectors), MPIfR A. Fletcher, R. Beck; Optical: NASA/Hubble Heritage, STScI; Graphics: Sterne and Weltraum.

reaching 20 μG. It is thought that higher turbulent gas velocities in the arm regions decreases the dynamo strength promoting greater field strength in the inter-arm areas. Magnetic fields are also observed in barred galaxies, and total field strengths correlate with the length of the bar. Edge-on galaxies display magnetic fields that are mainly parallel to their disks except in some galaxies with strong star formation and galactic winds.

2.10   Additional Reading

The listing is not intended to be comprehensive but will complement the text. Advanced texts or papers are indicated with the † symbol.

P. A. Charles and F. D. Seward, 2010, Exploring the X-ray Universe, 2nd Edition, (Cambridge University Press, Cambridge).

J. J. Condon, 1992, Radio Emission from Normal Galaxies, Annual Review of Astronomy and Astrophysics, **30**, 575.

L. C. Ho, 2008, Nuclear Activity in Nearby Galaxies, Annual Review of Astronomy and Astrophysics, **46**, 475.

R. C. Kennicutt, Jr., 1998, Star Formation in Galaxies along the Hubble Sequence, Annual Review of Astronomy and Astrophysics, **36**, 189.

I. Robson, 2009, The submillimetre revolution, Experimental Astronomy, **26(1-3)**, 65.

B. T. Soifer, G. Helou and M. Werner, 2008, The Spitzer View of the Extragalactic Universe, Annual Review of Astronomy and Astrophysics, **46**, 201.

†Longair, M.S. 2009, High Energy Astrophysics, Vols. 1 and 2, (Cambridge University Press, Cambridge).

†D. E. Osterbrock, 1989, Astrophysics of Gaseous Nebulae and Active Galactic Nuclei, (University Science Books, Mill Valley, CA).

†J. A. Peacock, 1999, Cosmological Physics, (Cambridge University Press, Cambridge), chapters 12-14.

†L. Spitzer, 1998, Physical Processes in the Interstellar Medium, (Wiley-Interscience, New York).

Gauss (1777-1855). The Earth's magnetic field measures about 0.5 gauss, and the surface of a neutron star has a field of about 10^{12} gauss